DRACO

Final Proposal
University of Maryland, College Park
Undergraduate Team

42nd Annual Vertical Flight Society
Student Design Competition
Pioneering Hydrogen-Electric VTOL

Sponsored by AIRBUS HELICOPTERS

Alfred Gessow Rotorcraft Center
Department of Aerospace Engineering
University of Maryland
College Park, MD 20742 U.S.A.

Alfred Gessow Rotorcraft Center
Department of Aerospace Engineering
University of Maryland
College Park, MD 20740 U.S.A

Sam Renz
Undergraduate Student (Team Captain)
srenz@terpmail.umd.edu

Billy Lee
Undergraduate Student (Transmission)
leeb2221@terpmail.umd.edu

Ron Berlin
Undergraduate Student (Aerodynamics)
rberlin8@terpmail.umd.edu

Isaiah Lee
Undergraduate Student (CAD)
ilee1234@terpmail.umd.edu

Colby Cotoia
Undergraduate Student (Aerodynamics)
ccotoia@terpmail.umd.edu

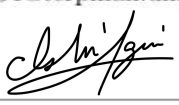

Ishmael Agui
Undergraduate Student (CAD)
iagui@terpmail.umd.edu

Joshua Katz
Undergraduate Student (Hydrogen System)
jkatz369@terpmail.umd.edu

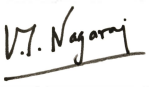

Dr. Vengalattore T Nagaraj
Faculty Advisor
vnagaraj@terpmail.umd.edu

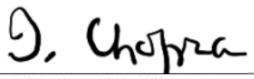

Dr. Inderjit Chopra
Alfred Gessow Professor
chopra@umd.edu

Students will receive credits for ENAE 482 (Aeronautical Systems Design) for their contributions.

Acknowledgements

The design team wishes to acknowledge the following people for their invaluable discussion, guidance, and support throughout the course of this project.

University of Maryland faculty and staff

Dr. Vengalattore T. Nagaraj - Research Scientist, Department of Aerospace Engineering

Dr. Inderjit Chopra - Alfred Gessow Professor and Distinguished University Professor, Director of Alfred Gessow Rotorcraft Center, Department of Aerospace Engineering

Dr. Anubhav Datta - Alfred Gessow Professor, Department of Aerospace Engineering, University of Maryland, College Park

Dr. James Baeder - Igor Sikorsky Distinguished Professor in Rotorcraft Professor, Department of Aerospace Engineering

Alfred Gessow Rotorcraft Center students

Logan Swaisgood

Vivek Uppoor

Sridatta Satuluri

Special thanks to:

Dr. Tomasz Krysinski - Visiting Scientist at the University of Maryland

John Piasecki - CEO and President of Piasecki Aircraft Corp.

Alfred Gessow Rotorcraft Center
Department of Aerospace Engineering
University of Maryland
College Park, MD 20740 U.S.A

To the Vertical Flight Society,

The members of the University of Maryland Undergraduate Student Design Team hereby grant VFS permission to distribute the Executive Summary and Final Proposal for the 42nd Annual Design Competition as it sees fit.

Best Regards,
The UMD Undergraduate Design Team

Contents

List of Figures

List of Tables

1 Introduction

The Vertical Flight Society's 42nd Annual Student Design Competition, sponsored by Airbus Helicopters, has tasked the 2024-2025 class with designing a hydrogen-electric VTOL. More specifically, this vehicle must travel from the Wright Brothers National Memorial in Kitty Hawk, North Carolina, USA, to the Alligator River, 30 kilometers away. Then, the vehicle must loiter for as long as possible and observe the species of animals present, before finally returning to the starting point. A more detailed breakdown that is categorized by mission segment is included in Section 3.3.

The University of Maryland Undergraduate Team is proud to present *Draco* as our response to the RFP of the 42nd Annual VFS Student Design Competition, shown below in Figure 1.1. *Draco* uses a simple, effective configuration: a single main rotor helicopter with compounded wings. Through calculations and trade studies, we were able to design a rotorcraft capable of performing the prescribed mission with maximized loiter endurance, while meeting all design constraints and requirements. Complete breakdowns of the RFP requirements and deliverables–and where to find our solutions–are included, in Table 1.1 and Table 1.2.

Figure 1.1: *Draco*

Hydrogen has seen a growing prevalence in recent years. Hydrogen fuel cells can be traced back to 1839, when William Robert Grove designed the first functional fuel cell, which used only hydrogen and oxygen to generate electricity. Then, during the 1960s, General Electric developed the first Proton Exchange Membrane (PEM) fuel cells for NASA's Gemini space program, which was notable for its low weight and high energy production relative to other forms of hydrogen-based energy. Commercial use of these fuel cells finally came to development by the 1990s, used in transit buses and cars. Significant government funding and private investments in this era enabled the continued development of this technology, and the rotorcraft industry has played a major role in this accelerated research into hydrogen-electric vehicles. In the midst of a changing global environment, companies and organizations are prioritizing renewable energy development to mitigate greenhouse gas emissions while improving energy efficiency and reliability. The aviation sector undoubtedly has high potential when it comes to sustainable development. As hydrogen storage and proton exchange membrane systems both develop further, the aerospace industry, especially vertical takeoff and landing vehicles, are meeting new milestones quickly. Recently, in August, 2024, Aurora Flight Sciences completed a successful 7-hour endurance flight of their unmanned hydrogen-electric VTOL, *SKIRON-XLE*, pictured in Figure 1.2 [1]. With various companies like Aurora, Piasecki, HyPoint, Sirius, and Urban Aeronautics developing new models of hydrogen-powered eVTOLS, students around the world are contributing to these designs further to aid in the research and design of hydrogen-electric VTOLs in this year's competition.

Figure 1.2: SKIRON-XLE by Aurora Flight Sciences

Table 1.1: RFP Compliance

RFP Requirement	Sections
Full-electric aircraft, powered by PEM fuel cells, with pressurized gaseous H_2 storage	5
Carry 1 pilot and 1 passenger with luggage, equivalent to a total payload of 185 kg	3
Complete aircraft with full rotor disk(s) must fit within a rectangular prism of dimensions 10 m x 10 m x 4 m	1,3,8
A minimum interior usable cabin floor dimension of 1.25 m (width) x 1.5 m (length)	1,8
The PEM fuel cell and all the associated systems must be carefully sized.	5
Reach a high-voltage (HV) network maximum of 840V	5
The PEM stack should not operate at a steady-state temperature of more than 90°C	5
The H2 tank pressure should not exceed 700 bar ($7x10^7$ N/m^2)	5
Hydrogen storage systems, high-temperature / low-temperature cooling systems, air and water management systems must be sized accurately and completely.	5
A particular focus must be placed on the physical integration of all these systems, with credible volume allocations and defined load paths for the airframe.	5,6,8
Airframe surface locations of air inlets and outlets must be provided in detail	8
If transient power limitations are identified due to fuel cell dynamic response, additional electrical supply devices should be considered.	3,5

Table 1.2: RFP Deliverables

RFP Requirement		Sections
Trade Studies	Vehicle configuration choice	3
	Rotor/Propeller design	3,4
	Powerplant selection	5
	Transmission design	6
	Wing design	3
	Fuselage design	8,12
Vehicle Performance Analysis	Total power required: all mission segments	3,5,10
	Vehicle aerodynamic power required (e.g., for a helicopter this would be rotor shaft power required) for all mission segments	3,12
	Electric motor(s) RPM- torque during the mission	6,12
	PEM Fuel cell efficiency, all mission segments	5,12
	Hydrogen flow rate and consumption during the mission	5,12
Performance Metrics	Maximum level flight speed at SL ISA, and constraints (required torque and power)	12
	Shaft power breakdown in trim with respect to speed	12
Airframe Aerodynamic Metrics	Drag area (D/q) at zero degrees pitch and yaw angle	12
	Pitching moment volume (M/q) at zero degrees pitch and yaw	12
	Drag estimation methodology	12
	Airframe Aerodynamic L/D	11
Vehicle drawings	Three-view external geometry	1,8
	Fuselage internal layout with center of gravity location	8
	PEMFC-related system drawings	5,8
Weight breakdown, center of gravity analysis, evolution throughout mission		8,11,12

Size Specifications

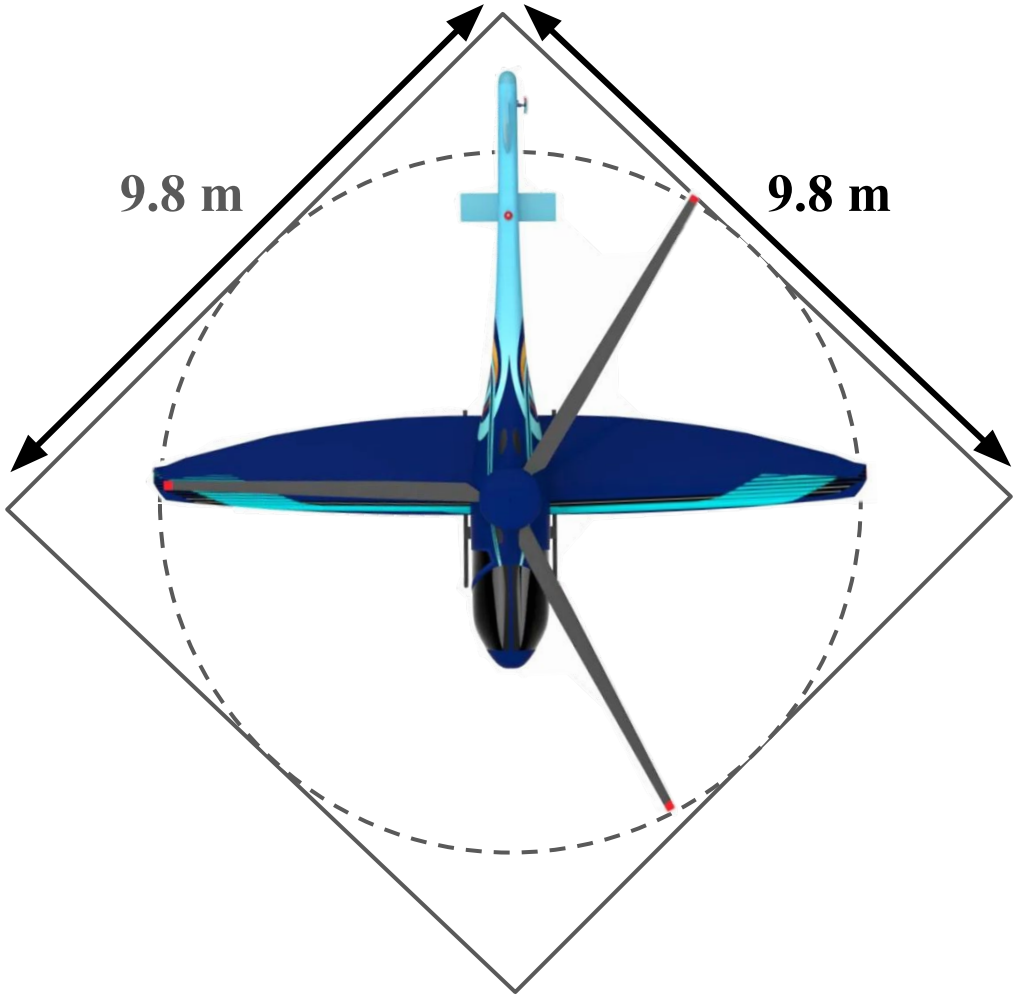

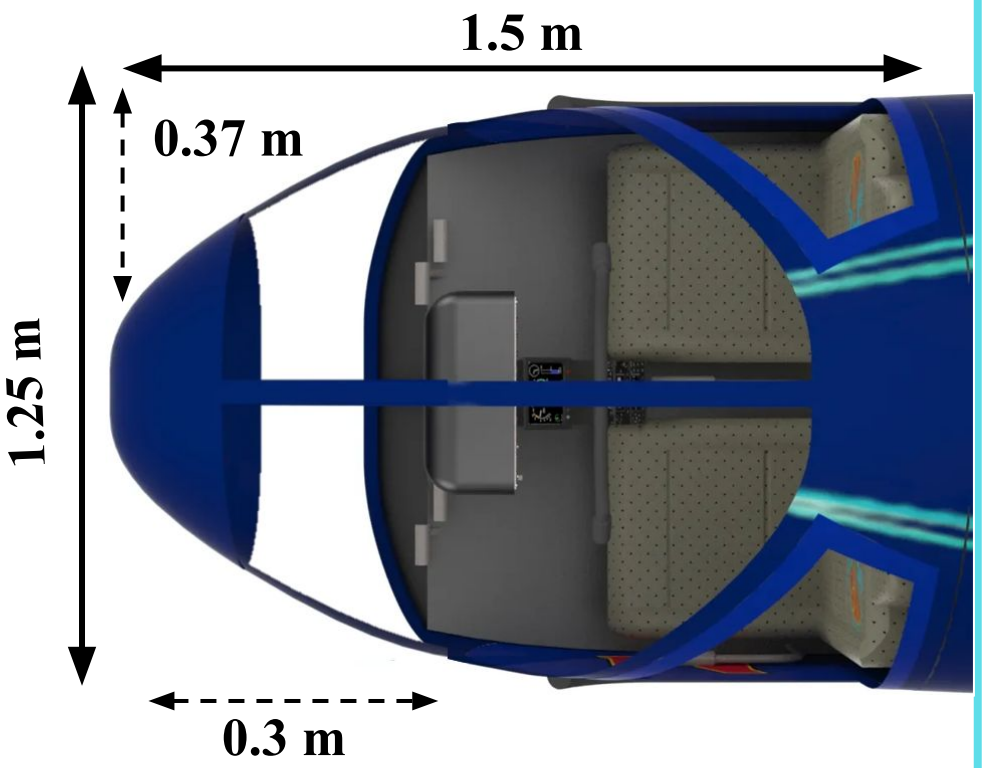

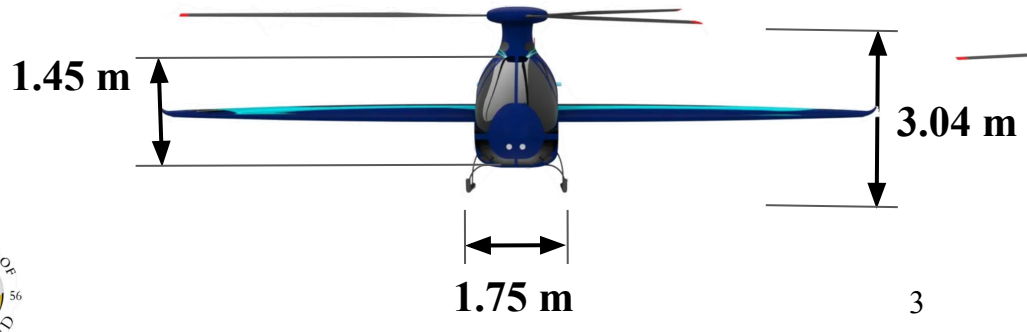

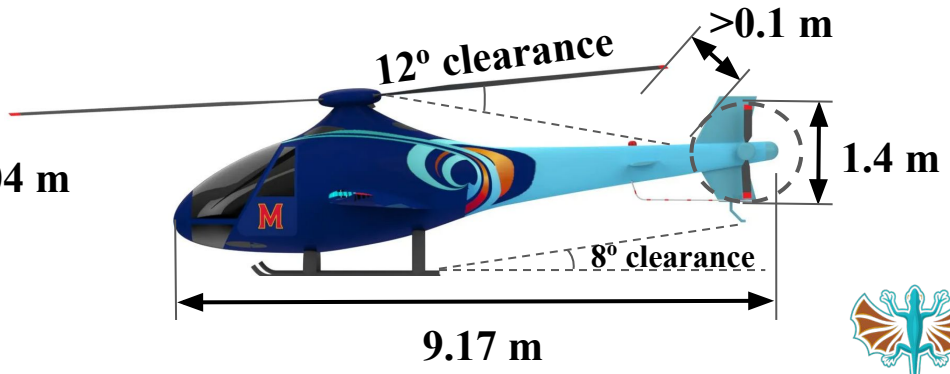

2 Configuration Selection

Draco is designed to maximize loiter time by maintaining a low empty weight fraction, avoiding mechanical complexity, and selecting a configuration that requires a relatively lower power consumption during cruise. This year's RFP calls for a hydrogen-powered VTOL with a specified mission profile to loiter for as long as possible. This loiter time is the central design variable we need to consider. We are also tasked with addressing and overcoming specific challenges of using hydrogen as a fuel source in passenger-carrying aircraft, making safety of major importance. Considering that this technology is relatively new to VTOL design, our design philosophy is to use proven, well-established design principles and simple, reliable systems.

Beyond the explicitly mentioned requirements, we must also consider the implicit design goals associated with our mission. Seeing that the goal of the loiter segment is to observe the wildlife in Alligator River, one of our priorities is to minimize the disturbances that would affect the observations, namely, noise. Then, in the spirit of maximizing loiter endurance, we must also reduce our overall power and fuel requirements by reducing the weight and creating a design that requires as few heavy mechanical components as possible.

2.1 Voice of the Customer

The RFP voices the customer's needs, so we translated those requests into design drivers to use in our Analytical Hierarchy Process (AHP). We categorized the design drivers as either "explicitly mentioned in the RFP" or "implicit design goals." The former pertains to criteria that the RFP directly imposed on us, while the latter includes design goals that we believe are important to ensuring a viable design for a successful mission. Within each category, the drivers are listed in order of importance, according to the results of our AHP.

2.1.1 Design Drivers: Explicitly Mentioned in the RFP

1. **Loiter Endurance:** To maximize our loiter time, we must keep power requirements low during the loiter segment of our mission to reduce our required hydrogen consumption rate. This can allow us to loiter for longer for the same mass of hydrogen.
    - *Section 2.2: Pioneering Mission* states, "loitering time must therefore be maximized."
2. **Safety and Reliability:** The safety of both the ground maintenance crew and the people on board. Safety concerns are a major design consideration when storing hydrogen at high pressure, so we must prioritize this highly for a passenger carrying aircraft.
    - *Section 2.1: Operating Concept* asks us to "understand and overcome the specific challenges and requirements of a passenger carrying hydrogen-powered VTOL aircraft."
    - *Section 1.5.2: Application and Feasibility* also asks us to "discuss how reliability and maintainability features influenced the design process."
3. **Minimized Life-Cycle Cost:** If our design is more affordable to manufacture and repair, it is more marketable and affordable to any clients.
    - *Section 1.5.2: Application and Feasibility* asks us to "discuss how affordability considerations influenced the design process."

2.1.2 Design Drivers: Implicit Design Goals

1. **Empty Weight Fraction:** The weight of the airframe, hub, and rotors as a fraction of the gross take-off weight. Keeping these weight values low will allow us to allocate more weight to hydrogen tanks and thus store more hydrogen, extending the endurance of the vehicle.
    - *Section 2.2: Pioneering Mission* states, "This loiter time must be maximized." A lighter vehicle needs less power and allows the fuel to last longer.
2. **Mechanical Simplicity:** Using the fewest parts necessary for our helicopter to function effectively. Keeping parts to a minimum can help reduce weight, and thus increase our endurance. Also, considering

the efficiency of each component, using fewer parts allows us to avoid as much energy loss and use as much of our generated power as possible.

3. **Acoustics:** Both the sound pressure level (loudness) and frequency of the noise we produce impact the wildlife to be observed. One priority is to keep the sound quiet and avoid frequencies near 1 kHz, alligators' peak hearing threshold.

    - *Section 2.2: Pioneering Mission* specifies that we are observing a place where "the chance of observing several very interesting species of animals is high." The observations should be kept accurate by minimizing disturbance to the wildlife.

2.1.3 Prioritizing Design Drivers

Implementing an AHP allows us to subjectively quantify the design drivers, scoring them by how important they are with respect to each other's design drivers. After selecting design drivers from the RFP, the voice of the customer, we organized them into a matrix in which each row or column represents a design driver. Then, for each cell, we assigned a score between 1/9 and 9, where scores above 1 indicate that the row design driver is more important than the column design driver, and vice versa for scores below 1. A score of 1 indicates equal importance, and scores further from 1 indicate increasing relative importance. For example, a score of 9 indicates that the row driver is *absolutely* more important than the column driver, but a score of 1/3 (0.33) indicates that the column driver is *slightly* more important than the row driver. Each team member completed this process individually, and the scores were averaged to consider every member's perception of the voice of the customer and avoid one-sided decision-making. Our AHP matrix is shown in Table 2.1.

Table 2.1: AHP: Design Driver Selection

Parameter	Loiter Endurance	Minimum Life-Cycle Cost	Mechanical Simplicity	Safety and Reliability	Acoustics	Empty Weight Fraction
Loiter Endurance	1	3.16	3.5	1.79	4.63	1.75
Minimum Life-Cycle Cost	0.32	1	0.71	0.49	1.33	0.29
Mechanical Simplicity	0.29	1.41	1	0.49	1.33	0.29
Safety and Reliability	0.56	1.94	1.22	1	2.68	1.5
Acoustics	0.22	0.76	0.51	0.37	1	0.33
Empty Weight Fraction	0.57	3.5	3.25	0.67	3	1

Based on the results of our AHP, **loiter endurance** is by far the most important design driver. Seeing as how our main goal is to maximize loiter time, this was expected. By this same logic, we felt it was also fitting that our second most important design driver is **empty weight fraction**. Not far behind is **safety and reliability**, which is vital for all passenger-carrying aircraft, especially when hydrogen is our fuel source. In summary, we need to maximize the loiter time without detrimentally increasing the vehicle's empty weight. Meanwhile, we need to ensure our vehicle uses hydrogen fuel cells as safely as possible, so we should make sure to guarantee that any increase in loiter time will not over-exert our fuel cell.

Table 2.2: Normalized Priority Vector

Design Driver	Weight
Loiter Endurance	32.56%
Empty Weight Fraction	22.30%
Safety and Reliability	19.03%
Mechanical Simplicity	11.12%
Life-Cycle Cost	8.42%
Acoustics	6.55%
Total	100%

Overall, the three aforementioned design drivers are the most vital, not only to our configuration selection but also to all design choices we have made. The three remaining drivers are not as crucial as the first, but we kept all six drivers in mind throughout the design process nonetheless because they are all relevant to a successful mission.

2.2 Candidate Configurations

Because hydrogen fuel cells are relatively new for VTOL design and have limited real-world examples, we made sure to only consider existing VTOLs as possible configurations. Figure 2.1 includes the configurations we considered, each paired with the example we used as a reference.

- **Single Main Rotor (SMR) and Tail Rotor:** We used the Guimbal Cabri as a reference for the baseline configuration of SMR with a tail rotor. This is the most mechanically simple and affordable design, and it avoids the added drag associated with compounded wings. However, its speed is limited, and all of its lift must be generated by the main rotor, so power requirements during cruise and loiter are high.
- **Lift Compounded SMR:** Despite the wider profile and added drag, a lift-compounded SMR may require less power generation for the main rotor by sharing some of its lift with the wings. We referred to the Bell 360 Invictus as an example.
- **Lift and Thrust Compounded SMR:** The example included is the Eurocopter X3, which has a single main rotor and a pair of main wings with pusher propellers. The propellers in this example produce different values of thrust to counteract the torque generated by the main rotor. This negates the need for a tail rotor, further simplifying the design.
- **Coaxial:** This configuration has two sets of rotors that spin in opposite directions along the same central axis. The rotor hub is more complicated than that of an SMR, but the two rotors produce torque in opposite directions and negate the need for a tail rotor. We used the EDM Aerotec Coax 2D as a reference.
- **Lift and Thrust Compounded Coaxial:** This configuration has two coaxial rotors, but adds on both wings and a pusher propeller. We used the Sikorsky X2 as a reference. This configuration is generally capable of higher speeds than SMR or coaxial designs without compounding.
- **Tiltrotor:** This configuration includes a pair of wings with a rotor mounted on each, and it allows us to lift off vertically and eventually tilt the rotors forward to produce horizontal thrust in addition to lift. Then, in cruise, this configuration can tilt the rotors all the way forward to generate a majority of the necessary lift from its wings and thrust from its rotors. The example we included is the Bell XV-15.
- **Tandem:** This configuration tends to be heavier than most other configurations we considered, but because it has two main rotors separated longitudinally and rotating in opposite directions, it produces a net zero torque and is also much more tolerant to changes in center of gravity. This configuration is fairly common, and the specific design we referenced was the Boeing CH-57 CHINOOK.
- **Quadcopter or Multicopter:** A configuration with four or more main rotors was considered because it is versatile, can be designed without a tail rotor, and is slightly tolerant to changes in center of gravity. The example we used as reference is the Workhorse SureFly, a passenger-carrying quad-rotor helicopter.
- **Lift and Cruise:** This type of configuration uses multiple rotors that can be used for either lift or forward thrust, and they can also be paired with wings to share some of the lift. Aurora has created the SKIRON-XLE, an unmanned VTOL that uses hydrogen fuel cells for propulsion, like our mission. This example is drastically lighter than any manned aircraft we will design, but it shows that this configuration can use the type of fuel system we are looking for.

2.3 Pugh Matrix

We included all of these configurations in a Pugh decision matrix, Table 2.3, which allowed us to condense our options into a select few configurations, which we then evaluated more precisely in our trade studies. In our Pugh matrix, each row represents a design driver, weighted according to the AHP matrix, and each column represents a configuration candidate. Thus, each cell is given a score that indicates whether the configuration is better or worse with regard to a single design driver.

Figure 2.1: Candidate Configurations

Starting from the simplest configuration, we treated the SMR as our baseline and thus assigned it a score of 0 for each design driver. Then, every other configuration was scored based on how it performs against the SMR, on a scale of -5 (extremely worse than SMR) to +5 (extremely better than SMR). Finally, each configuration received a score that is the sum of each of its design driver scores, multiplied by each design driver's weight. This is the dot product of the configuration's column and the normalized priority vector.

Table 2.3: Pugh Decision Matrix

Parameter	Weight	SMR	SMR Lift Comp.	SMR L+T Comp.	Coaxial	Coaxial L+T Comp.	Tiltrotor	Tandem	Quad.	Lift and Cruise
Loiter Endurance	0.33	0	2	3	1	2	3	-1	-1	2
Minimum Life-Cycle Cost	0.08	0	-1	-2	-1	-3	-2	-3	1	-1
Mechanical Simplicity	0.11	0	-1	-2	-2	-3	-4	-1	-1	-4
Safety and Reliability	0.19	0	-1	-1	-1	-1	-1	0	1	1
Acoustics	0.07	0	0	-1	-1	-2	-2	-1	-3	-2
Empty Weight Fraction	0.22	0	-1	-2	-2	-4	-3	-2	-2	-3
Score	1	0	0.06	-0.09	-0.67	-1.12	-0.6	-1.19	-0.82	-0.47

The highest-scoring configurations according to the design criteria are **Lift Compounded SMR**, **Classic SMR**, and **Lift and Thrust Compounded SMR**. Thus, these three configurations were selected for further detailed analysis through the trade studies discussed in Chapter 3.

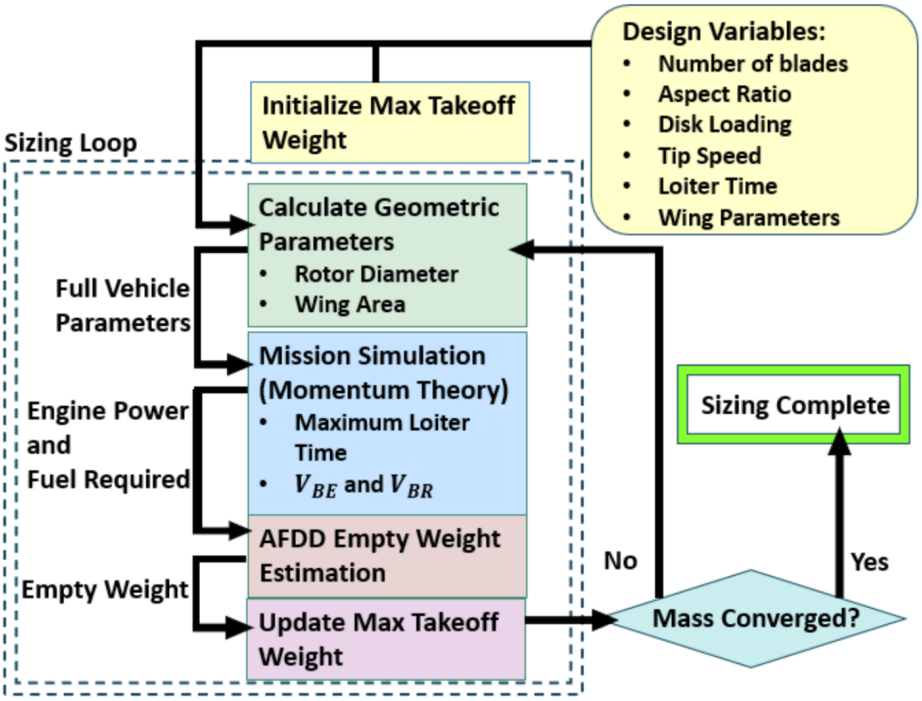

Figure 3.1: Sizing Methodology Flowchart

3 Preliminary Sizing

3.1 Sizing Methodology

Draco is intended to maximize loiter time with a low fuel and takeoff weight. For each iteration of our initial sizing, we set an initial gross takeoff weight and calculated the required blade and wing parameters. After simulating the mission with momentum theory, we predicted the maximum loiter time, best range speed, and best endurance speed. From this, we predicted power requirements and updated the maximum takeoff weight. If this value does not match our initial input, we repeat that process until the gross takeoff weight converges to a consistent value. This process is illustrated in Figure 3.1, and this allowed us to compare our best configuration options qualitatively.

3.2 Sizing Code Validation

An in-house sizing code was modified and validated using the Robinson R-44 data. The sizing code used a hypothetical flight mission to calculate the power required, fuel required, and component weights of the R-44 [2]. The hypothetical mission used to validate the sizing code is displayed in Table 3.1.

Table 3.1: Hypothetical Mission Profile

Mission Segment	Description
1	Ground Idle
2	HOGE for 60 seconds at 609.6 m (2000 ft), ISA +20°C
3	Climb to 1219.2 m (4000 ft) in 37.5 seconds, ISA +20°C
4	Cruise 160.9 km at 1219.2 m (4000 ft) in 1 hour, ISA +20°C
5	Descend to 609.6 m (2000 ft) in 60 seconds, ISA +20°C
6	HOGE for 60 seconds at 609.6 m (2000 ft), ISA +20°C
7	Reserve fuel for 20 minutes at V_{BE} at 609.6 m (2000 ft), ISA +20°C

For the given mission, the converged code outputs weights including takeoff weight, empty weight, fuel

weight, and other, more detailed, group weights. Empty weight groupings were calculated using U.S. Army Aeroflightdynamics Directorate (AFDD00) models from NDARC [3]. The sizing code iterates on rotor geometry values, installed power, and energy and fuel requirements. Performance functions including hover, cruise, climb, and descent, were used to calculate the power required per mission segment. The power requirements for each mission segment were then used to calculate energy and fuel requirements for the entire mission profile.

Table 3.2 presents the comparison of results of the sizing code with the corresponding data for the R-44 helicopter. The sizing code calculates the takeoff weight of the R-44 to be 1109.2 kg (2445.3 lb) while the true takeoff weight of the R-44 is 1106.77 kg (2400 lb), a -1.89% error. Similarly, the converged code calculates the empty weight to be 644.3 kg (1420.5 lb) while the true empty weight of the aircraft is 657.7 kg (1450 lb), a -2.03% error. The fuel weight of the R-44 was calculated to be 114.2 kg (251.8 lb), and the R-44's true fuel weight is 130.27 kg (287.2 lb), a 12.3% difference. No tech factors have been used to modify the AFDD weights. Despite this, the maximum difference between the actual and estimated values is 12.3%.

Table 3.2: Component Weight model Validation

R-44 Component	Actual Value	Code Estimation	Percent Error
Rotor Diameter [m (ft)]	10.016 (33.0)	9.95 (32.645)	+1.07%
Rotor System Weight [kg (lb)]	84.82 (187)	93.58 (206.3)	+10.3%
Fuel Weight [kg (lb)]	130.27 (287.2)	114.2 (251.8)	+12.3%
Fuselage Weight [kg (lb)]	142.43 (314)	133.72 (294.8)	+6.1%
Empty Weight [kg (lb)]	657.7 (1450)	644.3 (1420.5)	-2.03%
Takeoff Weight [kg (lb)]	1106.77 (2400)	1109.2 (2445.3)	-1.89%

3.2.1 Power Plant Comparisons from Sizing Code

To estimate the influence of power plant choice, two more configurations were selected using the same hypothetical mission profile and changing the power plant. Input parameters remained unchanged, such as the number of blades, disk loading, aspect ratio, and tip speed. These were applied as control variables for the power plant comparisons.

The turbine design has a Rolls-Royce RR300 engine which has a dry weight of 201 lbs and a power to weight ratio of 0.67 hp/lb [4].

The hydrogen fuel cell model assumes a specific fuel consumption of 0.0438 hp-h/lb and a power to weight ratio of 1.016 hp/lb [5].

Table 3.3 presents the weight and performance comparisons between the baseline design, the R-44 piston engine, the turbine engine, and the hydrogen engine designs.

Table 3.3: R-44 Weight Comparisons with Power Plant Variation

Weight Distribution	**Piston**	**Turbine**	**PEMFC**
Tip Speed [m/s (ft/s)]	214.88 (704.98)	214.88 (704.98)	214.88 (704.98)
Rotor Diameter [m (ft)]	9.95 (32.645)	9.72 (31.89)	21.55 (70.7)
Installed Power [kW (hp)]	157.9 (211.75)	150.63 (202.0)	944.73 (1266.9)
Rotor System Weight [kg (lb)]	93.6 (206.3)	88.0 (194)	707.5 (1559.8)
Fuel Weight [kg (lb)]	114.2 (251.8)	177.6 (391.6)	65 (143.4)
Engine Group Weight [kg (lb)]	203.2 (448)	102.5 (226)	1196.5 (2637.8)
Empty Weight [kg (lb)]	644.3 (1420.5)	529.9 (1168.3)	4788.1 (10556)
Takeoff Weight [kg (lb)]	**1109.2 (2445.3)**	**1058.2 (2332.9)**	**5203.6 (11472)**

The parameters common for all three variants are: a 2-bladed single main rotor with a disk loading of 2.98 lb/ft^2 (142.7 N/m^2), an aspect ratio of 18.679, and a main rotor tip speed of 214.9 m/s (705 ft/s). All engine variants were sized for the same hypothetical mission profile and payload requirements.

Given the range requirement in the assumed mission profile, fuel mass is the primary driver across engine configurations. The piston engine requires 114.2 kg (251.8 lb) of fuel to complete the mission. Transitioning to a turbine engine increases fuel consumption to 177.6 kg (391.6 lb)—a 55.5% rise—but this comes with a lower engine dry weight and represents a manageable, incremental change in overall design.

The shift to hydrogen power, however, introduces a radical departure from both piston and turbine configurations. Although the hydrogen-powered R-44 uses only 65 kg (143.4 lb) of fuel—a 56.9% reduction compared to the piston engine—the vehicle's empty weight skyrockets to 4,788.1 kg (10,556 lb). This is 9 times heavier than the turbine-powered design and 7.4 times heavier than the piston configuration.

This dramatic weight increase is driven primarily by the requirements of hydrogen storage and conversion systems. High-pressure hydrogen tanks have a high empty weight, and additional mass increases come from fuel cells, cooling systems, and supporting electronics. The transition to hydrogen is not just a change in fuel type—it fundamentally reshapes the aircraft's design, performance, and structural requirements in ways far beyond the piston-to-turbine shift.

3.3 Mission Profile of the RFP

As outlined in the RFP, the mission can be broken down into 16 segments, shown in Figure 3.2.

1. Normal vertical takeoff to HIGE at MSL
2. HIGE for 15 seconds at MSL
3. Vertical climb to 60 m above MSL (Vertical ROC = 0.76 m/s OGE)
4. HOGE for 10 seconds at 60 m above MSL
5. Steady climb to 300 m above MSL ($\gamma = 9°$)
6. Cruise at 300 m above MSL
7. Steep descent to 30 m above MSL (Vertical ROC = -7.6 m/s, autorotation considered)
8. HOGE for 30 seconds at 30 m above MSL
9. Loiter at 30 m above MSL at max endurance velocity
    - The objective is to maximize loiter time.
10. Steady climb to 300 m above MSL ($\gamma = 9°$)
11. Cruise at 300 m above MSL
12. Steady descent to 60 m above MSL (γ = -5°)
13. HOGE for 10 seconds at 60 m above MSL
14. Vertical descent to HIGE at MSL
15. HIGE at MSL
16. Normal vertical landing from HIGE

3.4 Trade Studies

Trade studies were conducted for a single main rotor, lift compound, lift and thrust compound, and a vectored thrust vehicle similar to the Joby S4. The input parameters define the rotor geometry, affecting the fuel weight and thus the total weight of the vehicle to complete the mission specified by the RFP. A Samsung 40T battery [6] was scaled to 25 kg (55 lbs), leaving a buffer of 5 kg for the required casing, which has an energy capacity of 5.14 kW-hr (6.9 hp-hr) and provides 57.9 kW (77.6 hp) in high power mission segments. Including a buffer battery allows the aircraft to significantly save on fuel stack system weight as it is no longer designed to solely reach the installed power requirement, which reduces the stack system weight and improves the loiter endurance. The total weight of the aircraft determines the power required and vehicle size. A more detailed explanation of the battery selection process is included in Section 5.

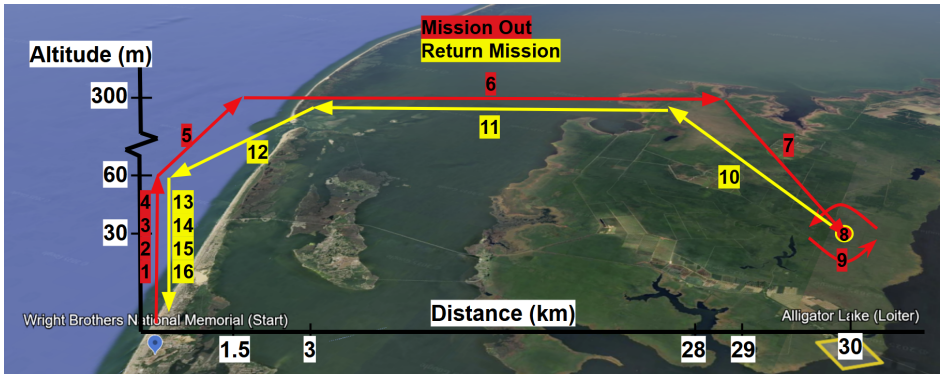

Figure 3.2: Mission Profile Segments

3.4.1 Blade Loading and Maximum Diameter

Blade loading (C_T/σ) is a non-dimensional measure of the lift coefficient of the rotor. Using the McHugh stall boundary [7], the beginning of the stall region is defined as $C_T/\sigma = 0.16$ in hover at sea level. $C_T/\sigma = 0.12$ is defined as the upper limit for this analysis to provide buffer room for maneuverability at higher altitudes. The RFP restricts the rotor diameter to less than 10 m (32.8 ft). To comply with the guidelines, all data points with $C_T/\sigma = 0.12$ or higher and maximum rotor diameter of 10 m (32.8 ft) were discarded when assessing plausible design specifications. However, the graphs displayed in the below section show all possible designs to display the proper data trends. For brevity, sizing of the lift compound configuration is shown below.

3.4.2 Number of Blades

The number of rotor blades (N_b) was varied from 2 to 5 while keeping the main rotor tip speed (V_{tip}) constant at $V_{tip} = 198$ m/s (650 ft/s) as well as a constant aspect ratio (AR) of 20. Figure 3.3(a) shows the effect on installed power with an increasing number of blades. Figure 3.3(b) shows the effect on loiter power with an increasing number of blades.

Minimizing the loiter power for a given loiter time minimizes the fuel and tank weight, decreasing the takeoff weight and installed power. A design with a high number of blades results in higher solidity for a fixed aspect ratio, increasing profile power and the mass of the rotor system. Therefore, we see installed power and loiter power decrease as N_b decreases. Fewer blades also simplifies the rotor hub, decreasing production costs and maintenance requirements of the aircraft. A two-blade rotor design is susceptible to mast bumping, so the design was avoided. From these considerations, $N_b = 3$ was selected.

3.4.3 Aspect Ratio

After selecting the number of blades, studies were directed to setting the blade aspect ratio (AR). Analysis was performed keeping $V_{tip} = 198$ m/s (650 ft/s) constant. Keeping the number of blades constant while varying the aspect ratio changes the blade loading. Because of this, a higher aspect ratio is generally more favorable when blade loading is a limiting factor.

The aspect ratio is a measure of the geometric solidity of the rotor. Number of blades is denoted by N_b and blade solidity is denoted by σ. For a rectangular-bladed rotor,

$$AR = N_b/\pi\sigma \tag{3.1}$$

Figure 3.4(a) shows the effect on installed power with a varying aspect ratio and disk loading. Figure 3.4(b) shows the effect on loiter power with a varying aspect ratio and disk loading.

As aspect ratio increases, decreasing disk loading is more impactful in decreasing power requirements. Increasing the aspect ratio higher than 20 is likely to pose structural complications and cause compressibility effects at the blade tip, so AR = 20 was selected for performance improvements.

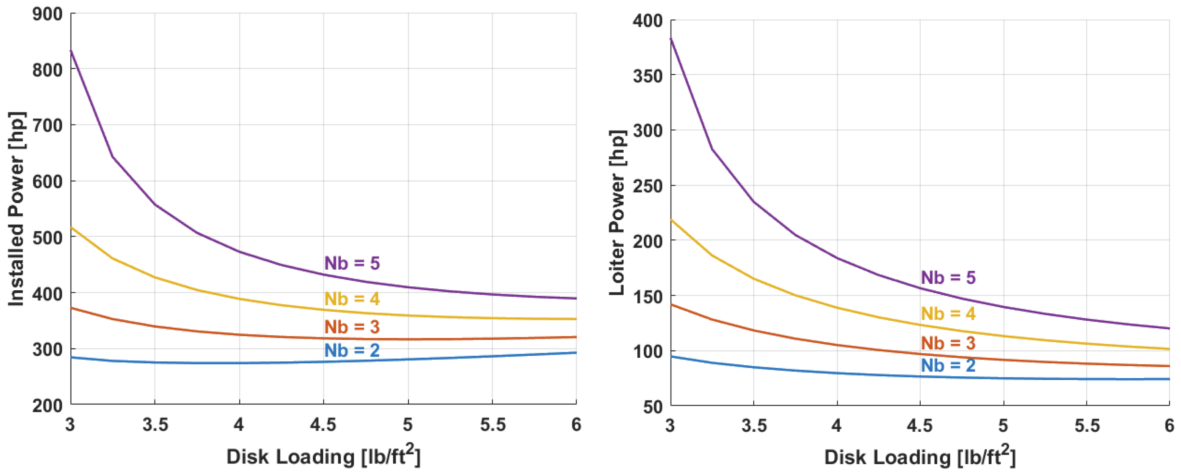

(a) Installed Power (b) Loiter Power

Figure 3.3: Tradeoff Study: Number of Blades

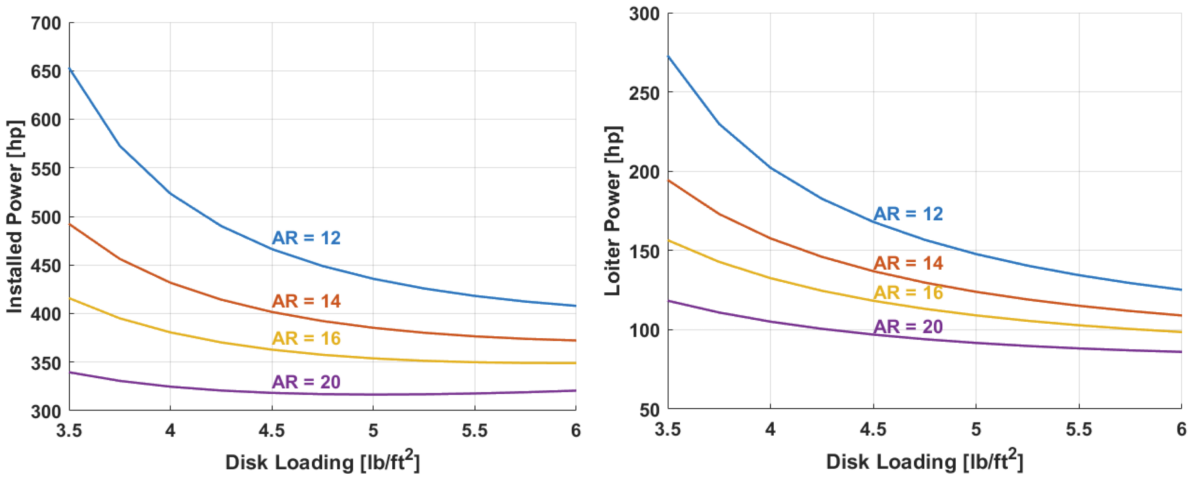

(a) Installed Power (b) Loiter Power

Figure 3.4: Tradeoff Study: Aspect Ratio

3.4.4 Main Rotor Tip Speed

With a determined number of blades and aspect ratio selected, fine-tuning the tip speed and disk loading will continue to lower the installed power of the helicopter and decrease takeoff weight. Main rotor tip speeds were chosen between 168 m/s (550 ft/s) to 228.6 m/s (700 ft/s), and disk loadings between 144 N/m^2 (3 lb/ft^2) to 287 N/m^2 (6 lb/ft^2).

The main rotor tip speed was not dropped in forward flight segments for the initial sizing of the vehicle. The best performance was found at DL = 206 N/m^2 (4.3 lb/ft^2) and VTIP = 198 m/s (650 ft/s). This resulted in a hover $C_T/\sigma = 0.0896$, allowing tip speed to be dropped 66% in loiter and cruise segments without exceeding $C_T/\sigma = 0.12$. Designing for a lower hover tip speed hindered the vehicle's total loiter time, as the main rotor could not be offloaded as efficiently in forward flight.

3.4.5 Wing Parameters for Lift Compounded Aircraft

Lift compounding a single main rotor aims to improve performance by offloading the main rotor when cruising. For the lift compounded design, wing sharing could not exceed 58.6% without exceeding a shaft tilt angle (α_s) of 8°. This limit was set to avoid an increase in fuselage flat plate drag and to ensure the wing

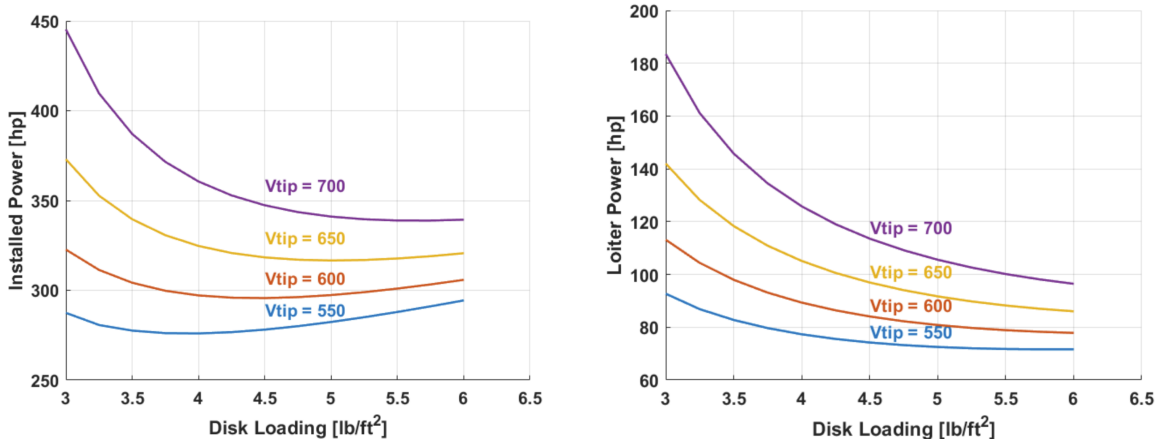

(a) Installed Power (b) Loiter Power

Figure 3.5: Tradeoff Study: Tip Speed

could continue to produce the required lift at a fixed incidence angle. This maximum shaft tilt of the lift compounded configuration is $\alpha_s = 7.68°$ at a forward range speed of 35.1 m/s (68.2 knots).

Figure 3.6 displays the wing geometry trade study. The wing aspect ratio was set to AR = 5 as it required the least amount of loiter power across all wing loading values. A wing loading (WL) value of 575 N/m^2 (12 lb/ft^2) was set. Lower wing loading values would result in wing areas that were too large to suit the aircraft's geometric constraints, and higher wing loading values would result in a loss of efficiency in cruise.

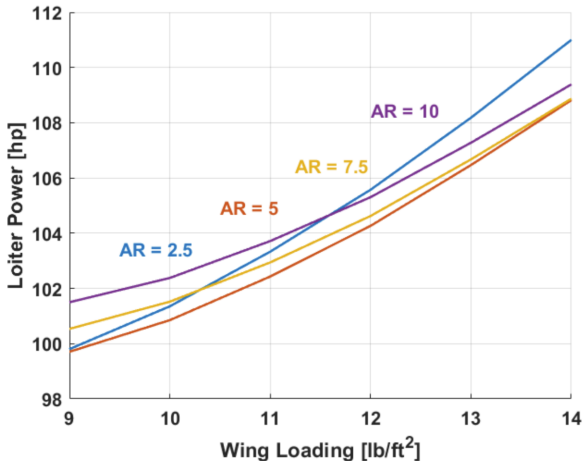

Figure 3.6: Trade Study: Wing Aspect Ratio and Wing Loading

3.4.6 Trade Summary

The three configurations considered are compared in Table 3.4. The power velocity curve is shown in Figure 3.7. All configurations were maximized for loiter time with similar disk loading values. The power velocity curve does not extend to the maximum installed power of the vehicle, since this occurs in the vertical climb segment of the mission.

The single main rotor and compound helicopter configurations all share similar disk loadings and takeoff weights. The maximum loiter time increases as the wing sharing factor increases, due to an offloaded main rotor and improved L/D with the use of a wing. The SMR configuration could only drop tip speed to 88% of the hover tip speed, without exceeding blade loading limits. Because of its higher power requirement in

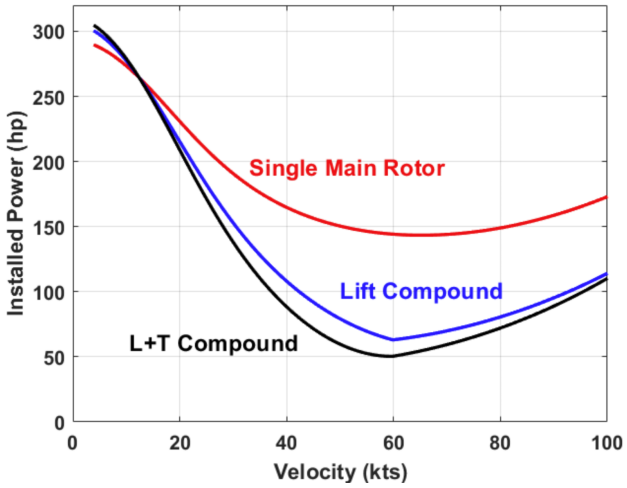

Figure 3.7: Power Velocity Curve for Top Configurations

loiter, loiter time is limited to 82 minutes with the single main rotor, so the configuration was discarded.

Lift compounding as well as lift and thrust compounding designs are both capable of reducing the tip speed in cruise segments to 66% of the hover tip speed. The lift compounded configuration is constrained to a maximum shaft tilt angle, as the main rotor is responsible for propulsive thrust. The lift and thrust-compounded design avoids this issue, with a pusher propeller providing the required propulsion.

The lift and thrust compounded design comes with a significant increase in mechanical complexity, compared to the lift compounded design. Increasing the mechanical complexity contributes to more points of failure in the design as well. The designed loiter speed was found to be around $V_{BE} = 30$ m/s (58 knots) for both the compounded rotorcraft that were considered. Pusher propellers are needed for a vertical takeoff and landing aircraft with high speed demands. Due to a low loiter speed, there is no need for a pusher propeller, and it would contribute to added mass near the aft portion of the aircraft, complicating balancing the center of gravity. Due to this, the lift and thrust compound configuration was ruled out.

The lift-compounded design was selected as it displayed a balance between a relatively high loiter time and mechanical simplicity. It showed a 34.2% increase of loiter time from the SMR. Despite a 2.4% decrease in loiter time from the lift and thrust compounded design, less failure points improves reliability and maintenance requirements. This made the lift compounded design more suitable for a sightseeing manned rotorcraft.

Details of the chosen configuration, *Draco*, are shown in Table 3.5, which includes a loiter time calculated in Section 12: Vehicle Performance.

Table 3.4: Vehicle Configuration Comparison

Parameters	SMR	Lift Compound	Lift+Thrust Compound
Disk Loading [N/m^2 (lb/ft^2)]	206 (4.3)	206 (4.3)	208 (4.35)
Number of Blades	3	3	3
Blade Aspect Ratio	20	20	20
Rotor Solidity	0.048	0.048	0.048
Rotor Hover Tip Speed [m/s (ft/s)]	198 (650)	198 (650)	198 (650)
Hover Tip Mach Number	0.58	0.58	0.58
Rotor Radius [m (ft)]	4.9 (16.1)	4.9 (16.1)	4.9 (16.1)
Wing Aspect Ratio	N/A	5	5
Wing Loading [N/m^2 (lb/ft^2]	N/A	575 (12)	575 (12)
Max Wing Share	N/A	58.6%	80%
Hover Download Factor	6%	12%	15%
Gross Takeoff Weight [kg (lb)]	1481 (3266)	1417 (3124)	1383 (3049)
Installed Power [kW (hp)]	253 (340)	254 (341)	257 (345)
Loiter Time (minutes)	94	127	130

4 Main Rotor Blade Aerodynamic Design

The design of our rotor blade geometry was optimized to maximize the Figure of Merit (FM) in hover as well as the Lift-to-Drag ratio (L/D) in forward flight. Having two conflicting local optima proved to be challenging when deciding on a final design, but using a weighted prioritization of these two metrics and systematically breaking down what proved to be the most advantageous blade qualities made the process more straightforward.

4.1 Aerodynamic Design Objective

Given that the primary objective of our mission is to maximize loiter time, the aircraft will predominantly operate in forward flight. Optimizing L/D, therefore, becomes highly prioritized, as it directly impacts the efficiency of the vehicle in cruise. To evaluate the performance of each rotor configuration, the velocity of maximum range from preliminary sizing was used to determine L/D, since this performance metric will be maximized at this speed. While L/D is the primary focus for forward flight, it is essential not to overlook the Figure of Merit, since the rotor system must also be capable of efficient hovering during specific mission phases. To balance these two conflicting metrics, we plot the L/D and FM for each configuration to generate a Pareto frontier, which allows for the identification of the optimal trade-offs between hover performance and forward flight efficiency.

4.2 Design Space

We chose to narrow down our design space to 9 parameters for the blade geometry. These parameters included inner and outer twist, twist transition, inner and outer taper, taper transition, inner and outer airfoil, and airfoil transition. The range of values for each parameter is shown in Table 4.1. To calculate the efficiency metrics for each possible configuration in this design space is not computationally feasible, so we first looked to understand the general behavior of systematically altering each parameter. Making slight adjustments in one parameter while holding the others constant to visualize the trend in FM and L/D (Figure 4.1) will allow us to narrow down the design space to a more manageable size for computation.

Table 4.1: Complete Design Space

Geometric Variables	Lower Bound	Upper Bound
Inboard Twist Rate (deg.)	1	20
Outboard Twist Rate (deg.)	1	20
Twist Junction (r/R)	0.1	0.9
Inboard Taper Ratio	1	5
Outboard Taper Ratio	1	5
Taper Junction (r/R)	0.1	0.9
Airfoil	RC-10, RC-12, MH60, OA209, SSCA09, VR15, VR12, OA212, SC1012RS, SC1095	
Airfoil Transition (r/R)	0.1	0.9

Table 3.5: *Draco* Size Specifications

Parameters	*Draco*
Disk Loading [N/m^2 (lb/ft^2)]	206 (4.3)
Number of Blades	3
Blade Aspect Ratio	20
Rotor Radius [m (ft)]	4.9 (16.1)
Rotor Solidity	0.048
Rotor Hover Tip Speed [m/s (ft/s)]	198 (650)
Rotor Cruise Tip Speed [m/s (ft/s)]	130.7 (429)
Hover Blade Loading	0.0896
Wingspan	11.25 (36.9)
Wing Loading [N/m^2 (lb/ft)^2]	575 (12)
Wing Share in Loiter	49.4%
Wing Share in Cruise	58.6%
Hover Download Factor	12%
Fuel Weight [kg (lb)]	14.8 (32.6)
Gross Takeoff Weight [kg (lb)]	1417 (3124)
Installed Power [kW (hp)]	254 (341)
Loiter Time (minutes)	190.3

A controlled baseline configuration was specified before proceeding with altering parameters for analysis. Starting our blade design with a taper ratio of one, we first analyzed the metrics of 10 different airfoils without a bi-airfoil configuration to capture the full effect of each shape. The results of this preliminary airfoil evaluation showed that increases in FM and L/D coincided for different airfoils, so that particular geometries were superior in both metrics. The most efficient airfoil in this analysis was kept as the controlled airfoil for the proceeding examination of twist and taper efficiency trends.

Twist was then altered for trend analysis using this controlled airfoil and taper ratio of one. Only twist configurations presumed to be structurally and conceptually feasible were plotted and compared. This excluded configurations where the twist rate causes the blade to twist in the positive direction at any spanwise length rather than the negative direction. A constant linear twist rate of 12° was chosen from the analyzed twist configurations as the controlled twist for taper analysis because it exhibits fair FM and L/D metrics.

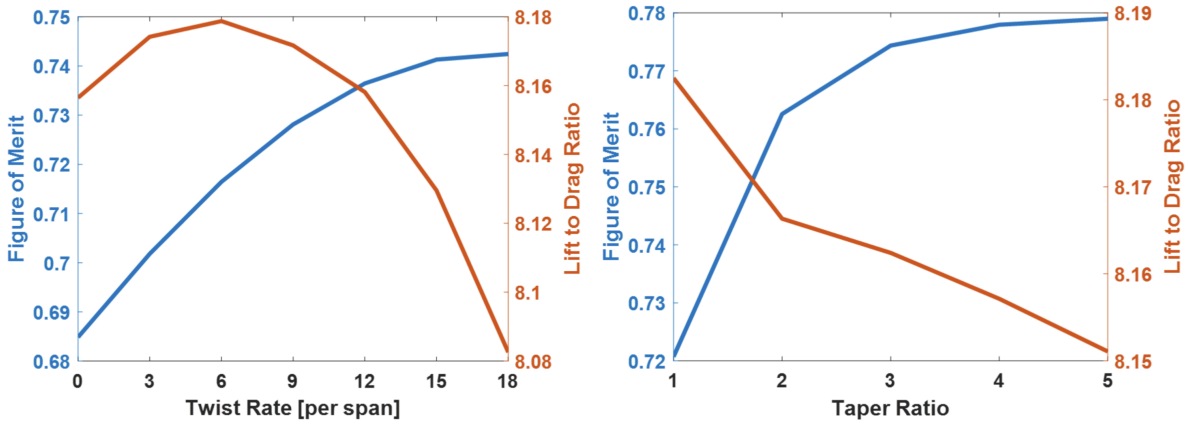

(a) Twist (b) Taper

Figure 4.1: Baseline Trade Study of FM and L/D vs. Twist and Taper

4.3 Navigating Tradeoffs

The results in Figure 4.1 show that higher twist rates result in increases in FM while lower twist rates result in increases in L/D. Similarly, higher taper ratios result in increases in FM while lower taper ratios result in increases in L/D. The results from this preliminary evaluation have allowed us to narrow down our design space significantly, as shown in Table 4.2, by prioritizing geometric variable ranges where vehicle L/D appeared most optimal. The three best airfoils from the preliminary airfoil evaluation were chosen for the entire spanwise cross-section for deeper analysis of these airfoils at different twists and tapers. Since the efficiency metrics demonstrate a negative correlation for varying twists and for varying tapers, a definitive design can not be immediately selected.

Table 4.2: Reduced Design Space

Geometric Variables	Range
Inboard Twist Rate (deg.)	3-9
Outboard Twist Rate (deg.)	3-9
Twist Junction (r/R)	0.25-0.75
Inboard Taper Ratio	1-3
Outboard Taper Ratio	1-3
Taper Junction (r/R)	0.45-0.95
Airfoil	OA-212
	RC-12
	VR12

Our new design space, plotted in Fig. 3.2, includes 4,251 designs representing the range of twists and tapers from Table 4.2, except for the exclusion of outboard twist rates being larger than inboard twist rates, as this would result in multi-directional twist along the blade span. The RC-10 airfoil is used for all configurations at the blade tip because of its thinner profile, which will help avoid transonic effects in forward flight and its high lift to drag ratio compared to airfoils of similar thickness. Vehicle lift to drag ratios are now calculated at the velocity of best endurance so that the main rotor can be optimized for the longest possible flight time in loiter.

Figure 4.2: Pareto Frontier Formed by Plotting FM vs. L/D

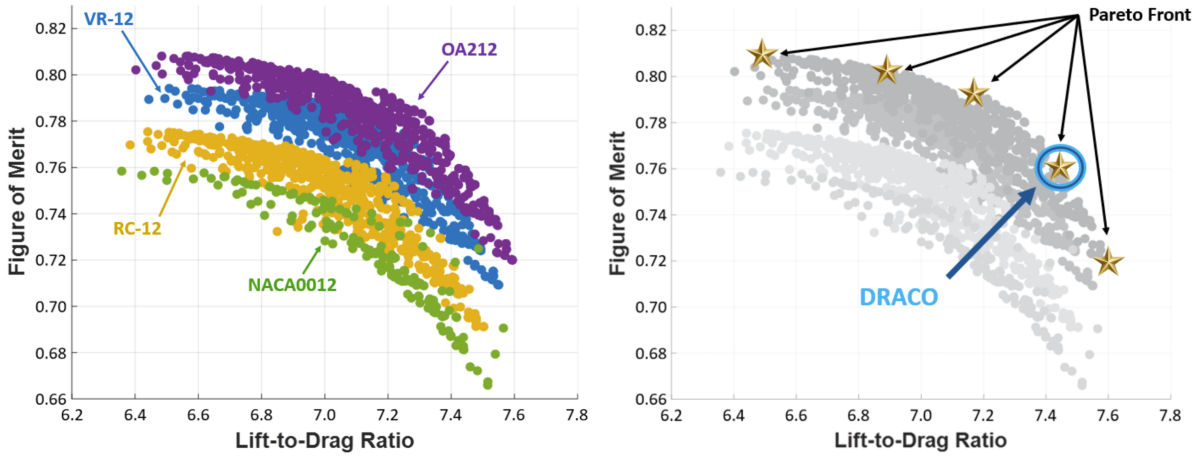

(a) Airfoil Comparison

(b) Design Comparison

The Pareto plot clearly reveals configurations that can be categorized as "dominant" or "non-dominant." Dominant configurations lay along the outer boundary of the Pareto front, represented by gold stars in Figure 4.2b, where no other configuration can improve either FM or L/D without compromising the other. In contrast, non-dominant configurations are located within the interior of the Pareto front. These are less favorable for our design, as there are other possible configurations that offer higher efficiencies without a tradeoff.

To pick the optimal configuration for our design, we observed how prioritizing L/D over FM affects our total energy consumption by comparing the optimal configuration for each efficiency metric. Both blade designs utilized an OA-212 airfoil cross-section with unique twists and tapers. The configuration that prioritized L/D boasted a 21.5% increase in Lift-to-Drag ratio but a 10.4% decrease in Figure of Merit as compared to the other design extreme that prioritized FM. Since our design priority is to optimize L/D without severely degrading our hover performance, we chose an effective design that performs above the 80th percentile in forward flight and 60th percentile in hover. Our final main rotor specifications for Draco are shown in Table 4.3, and the spanwise geometry is shown in Figures 4.4 and 4.5.

Geometric Variables	Optimized Values
Inboard Twist (°)	-7
Outboard Twist (°)	-6
Twist Junction (r/R)	0.3
Inboard Taper	1
Outboard Taper	2
Taper Junction (r/R)	0.5
Airfoil	OA-212
Outboard Airfoil	RC-10
Airfoil Transition (r/R)	0.8
Performance	**FM = 0.765** **L/D = 7.45**

Figure 4.3: *Draco*'s Optimized Rotor Blade

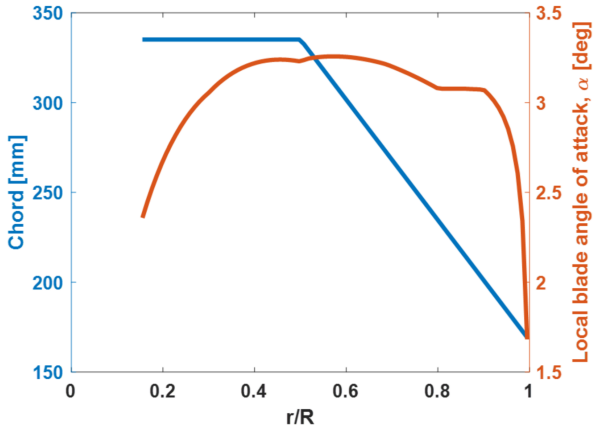

Figure 4.4: Optimized Main Rotor Geometry

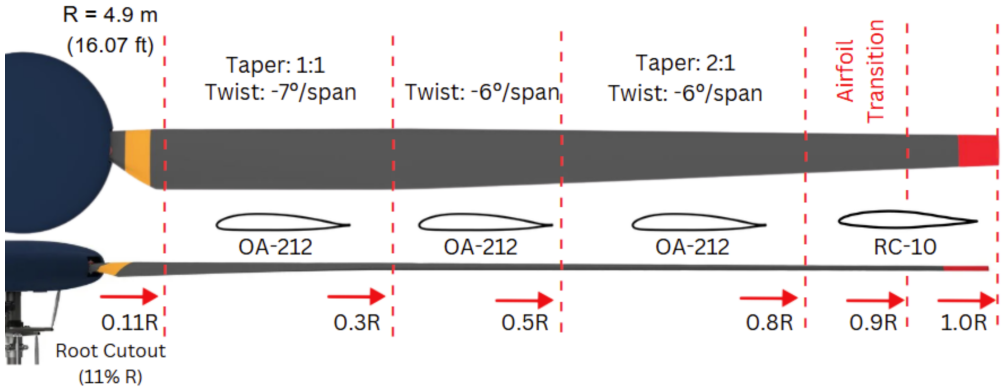

Figure 4.5: Profile of Optimized Main Rotor Blade

5 Proton Exchange Membrane Fuel Cell (PEMFC) System Design

5.1 Design Parameters

5.1.1 Methodology

Our design of the fuel cell is based on the methodologies detailed in NASA TR 20210000284 [8].

The design of the Proton Exchange Membrane Fuel Cell (PEMFC) involves sequentially sizing the fuel cell stack, hydrogen system, air system, cooling systems, water system, and electrical system to meet specified power requirements at minimum weight or a specified stack efficiency.

The software structure of the NASA report [8] organizes design variables into a single fuel cell data structure (FCST) and operational variables into a fuel cell operation structure (FCOP). Integration with aircraft design workflows requires only the provided input-output file (fcvariables.m) and these two structures. Several pre-configured run directories are included for baseline and modern system designs at different power levels.

5.1.2 Validation

We validated our parameters by comparing them to the outputs provided in the 80 kW Baseline example [6]. This comparison ensures that our results are both accurate and reliable, as it aligns our calculations with established benchmarks. By confirming that our parameters produce outputs consistent with those in the technical report, we can confidently rely on the validity of our model and its predictions.

The minimum weight design produces a stack with the design power as the maximum power. The maximum

power is the continuous power. For this option, the cell operates at the maximum power density, hence at a low voltage, and therefore at a poor efficiency. In this case, the input option for design power (ioptp) is set equal to 1.

The high efficiency design produces a stack that generates the design power at a specific cell voltage vc, that is optimized for a stack of high efficiency. In this case, the input option for design power (ioptp) is set to 3. For further explanation, see Section 10, "List of inputs and outputs" [8].

To validate our results, we compared the results of our analysis to the Horizon VLS-II-150 [5], a commercially available PEMFC system. The results are shown in Table 5.1.

Table 5.1: Comparing NASA Fuel Cell Design with Real Fuel Cells

	Horizon FC	**NASA Model FC**	**% Difference**
Rated Power [kW (hp)]	150 (201.15)	150 (201.15)	0%
Peak Power [kW (hp)]	165 (221.27)	164 (219.93)	-0.61%
Number of Cells	500	428	-14.4%
Voltage (V)	300	300	0%
Current (A) at P=150kPa	500	546	9.2%
Stack Power Density [kW/L (hp/ft^3]]	4.2 (159.5)	3.2 (121.5)	-23.8%
Stack Specific Power [kW/kg (hp/lb)]	2.5 (1.52)	2.53 (1.54)	1.2%
Volume with Casing [m^3 (ft^3)]	0.093 (3.28)	0.0867 (3.06)	-6.77%
Weight with Casing [kg (lb)]	78.8 (173.7)	97.9 (215.8)	24.2%
Fuel Consumption at P=80kPa	$\leq$ 0.73 m^3/kWh	0.00378 m^3/kWh	N/A
Stack Efficiency at P=80kPa	47.80%	47.32%	-1%
Operating Temp. °C, Stack	70-85	80	N/A
Operating Temp. °C, Env	-30-50	15	N/A

The results from the code [8] correlate closely with those of the Horizon VLS-II-150. The maximum percent difference is 27.8%, which occurs particularly due to the slightly heavier stack weights estimated by the hydrogen sizing code [8]. This consistency validates that the hydrogen sizing data calculated by the code is not only accurate but also technologically feasible, according to the current market availability of Proton Exchange Membrane Fuel Cell Systems.

5.2 PEMFC System Sizing

5.2.1 *Draco* Power System Overview

For PEMFC System sizing, we implemented the NASA code [6] for our specific design requirements. We used the Modern Liquid Cooled System as it provided the highest efficiencies in contrast to the Baseline or Modern non-liquid cooled systems. As inputs for the sizing code, the system was configured at the input option for design power (ioptp) set to 3. This will create a system at the specified cell voltage (v_c) of 0.67 V, that is optimized for a stack of high efficiency n. A design power of 122 kW was determined as the minimum value that will provide a maximum power of 196.58 kW after its Balance of Plant, as required by aerodynamic sizing, as the installed power.

Our PEMFC system does not require a low-temperature (LT) cooling system due to several key design decisions that simplify thermal management and reduce overall system complexity. First, the fuel cell stack is operated at atmospheric pressure (1 atm), eliminating the need for a high-pressure air compressor. In many fuel cell systems, the compressor and its intercooler represent major sources of heat that require dedicated low-temperature cooling; without these components, one of the primary drivers for an LT loop is

removed. Additionally, the stack is designed to operate efficiently at elevated temperatures, with a nominal temperature of 80°C and a maximum of 85°C for sizing purposes. This high operating temperature allows the entire stack and supporting components to be thermally managed using a single high-temperature (HT) cooling loop, without exceeding the thermal limits of the components.

Moreover, our balance-of-plant (BOP) components, including the air blower, humidifier, and power electronics, were selected with thermal tolerances that are compatible with the high-temperature loop. As a result, there is no need for a separate cooling circuit to maintain a lower coolant temperature for sensitive equipment. Eliminating the LT loop reduces system mass, power consumption, and failure points, which is especially advantageous in weight-sensitive applications such as aerospace systems. The simplification also improves reliability and streamlines integration, making the single-loop HT cooling strategy both effective and efficient for our PEMFC configuration.

The following section will exhibit the major outputs and sizing parameters of our hydrogen power system, as well as explain the design choices made when executing the sizing software and sizing balance of plant components. The main driver of this process was reliability and safety, therefore only market-available and proven components were selected.

The system will also be able to throttle both air flow and hydrogen flow according to power needs, so Draco can consume less fuel during forward flight and extend its endurance. As shown in Figure 5.2, the hydrogen flow rate can be reduced by about 70% in loiter compared to the installed power, which is needed for hover and vertical climb.

5.2.2 PEMFC Stack Sizing

The Stack was simulated and sized using the theory and Matlab code outlined in the NASA report [8]. We modified the 500 kW modern liquid-cooled system to match *Draco*'s power demands. Using this code, we input key mission data, including our maximum altitude of 300 m (984.25 ft) and maximum operating temperature of 80°C, a small safety margin cooler than the maximum allowed by the RFP. Because our stack needs to reach a maximum net power output of 196.58 kW, we input a "design power"—that is, the maximum efficiency power for this particular design—of 122.2 kW (163.9 hp). In addition, we sized our stack to operate with an air pressure of 1 atm, or 101.325 kPa (14.7 psi); this way, *Draco* utilizes surrounding air with a blower rather than stored air with a compressor. This change also eliminates *Draco*'s need for a low-temperature cooling system, which reduces our PEMFC system weight and volume further. Finally, we set our maximum fuel cell stack voltage to 400V. Because stack length is directly proportional to voltage, this upper voltage limit ensures our stack is short enough to size a cabin around without sacrificing aerodynamic efficiency.

Technology factors for cooling and air systems were adjusted accordingly to match our component selections later in our analysis.

A stack sized to a specified design power of 122.2 kW using the maximum efficiency design (ioptp =3), yields

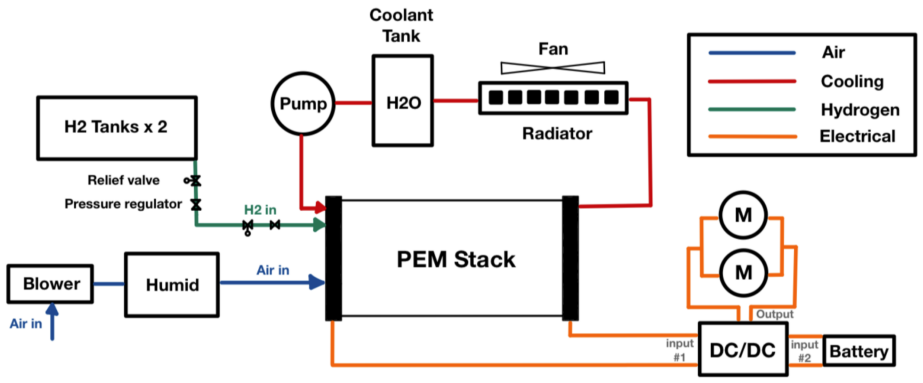

Figure 5.1: *Draco*'s PEMFC System Schematic

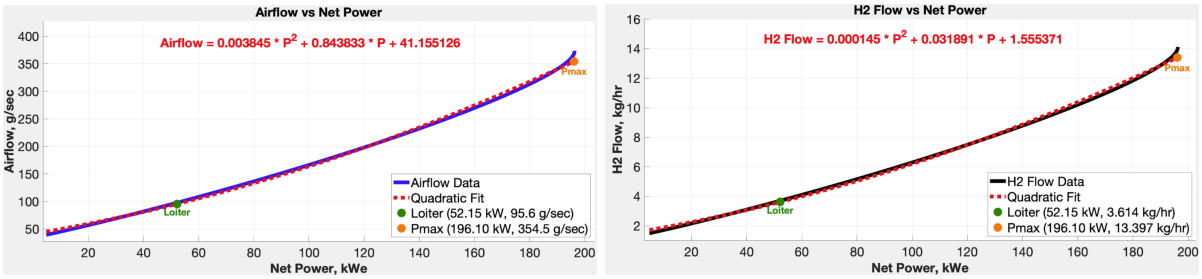

(a) Airflow Requirements (b) Hydrogen flow Requirements

Figure 5.2: Throttled Flow of Air and Hydrogen According to Power Demand

a stack system capable of throttling up to a maximum net power of 196.58 kW.

This will be sufficient for our design as we require a maximum stack output of 196.58 kW for Vertical climb (mission segment 3). This output estimates the weight of a stack of these specifications to be approximately **89.6 kg** (197.53 lb), excluding its enclosure.

The selected fuel cell stack is modeled after existing technology to ensure realistic application and feasibility. We focused on the Horizon VLS II-150, a market-ready PEMFC with high power output and an IP67-rated enclosure for dust and moisture resistance [5]. This model delivers 150 kW (201.15 hp) nominally and a maximum power of 165 kW (221.27 hp). At a weight of 84.7 kg (186.73 lb), it has a specific power of 1.95 kW/kg (1.185 hp/lb). From this, we were able to use our stack's maximum power output and specific power to extrapolate its mass, including its casing, as 100.8 kg (222.23 lb). Thus, the stack enclosure accounts for 11.2 kg (24.82 lb), or 11.1% of the total stack weight.

Based on the fundamental equations of hydrogen fuel cells outlined in the NASA report [8], we also designed our stack to have 597 cells, a volume of 0.072 m^3 (2.54 ft^3), a length of 1.54 m (5.05 ft), and a cross-sectional area of 0.05 m (0.16 ft). This sizing is crucial information to ensure our system can realistically be implemented into our vehicle, and this allows for credible allocation of volume in our cabin.

5.3 Cooling System Sizing

Although the fuel cell stack is nominally designed to operate at 80°C, we allowed it to reach 85°C during thermal load analysis. This decision reduces the size and weight of the radiator and associated cooling components while maintaining safe operation under the maximum temperature limit of 90°C prescribed by the RFP.

At full power output, the fuel cell stack generates a gross heat of 304.28 kW (408.05 hp), with the following losses subtracted: 24.49 kW (32.84 hp) from the air inlet, 22.01 kW (29.52 hp) from the air exhaust, 1.83 kW (2.45 hp) from convection losses, and 4.1 kW (5.5 hp) from radiation losses. Thus, we sized the radiator to counter a net heat load of 251.85 kW (337.74 hp).

5.3.1 Radiator Design

We used the convective heat transfer equation, with h_{rad}=2400 W/m^2K, T_a=15° C, and T_{rad}=(85° C+60° C)/2 =72.5° C. This yielded a required radiator surface area of 1.825 m^2 (19.64 ft^2).

To reduce the weight and size of the cooling system while maintaining adequate thermal performance, we applied a compactness factor (f_c) of 20 in our radiator design [9]. This factor accounts for the increased surface area achieved through finned or microchannel structures commonly found in compact heat exchangers [10] which typically have surface area densities ranging from 1000 m^2/m^3 (304.8 ft^2/ft^3) to 6000 m^2/m^3 (1828.8 ft^2/ft^3). When scaled to core depths of 3–10 cm, these heat exchangers have compactness factors ranging from 10 to 60. Thus, selecting a conservative value of 20 is both realistic and justifiable based on commercial radiator design practices. The frontal area of the radiator is therefore 0.09 m^2 (0.97 ft^2).

In addition to compactness, we assumed a frontal area density of 65 kg/m^3 based on surveyed specifications

of automotive-grade aluminum radiators and heat exchangers [11]. This value balances structural integrity and thermal performance while maintaining a reasonable mass.

The gives a radiator weight, W_{rad} of 5.93 kg (13.07 lb).

We calculated the radiator thickness based on proportionality from a similar market available component, resulting in an estimated thickness of 70.83 mm (2.79 in), which aligns with realistic packaging constraints for aerospace or mobile applications.

5.3.2 Coolant and Tank

Using the sensible heat formula, assuming water was used as the coolant with C_p = 4,180 J/kgK, and a temperature drop of 25°C, the required coolant mass flow rate, w'_{cool} was estimated to be 2.41 kg/s (5.31 lb/s). This corresponds to a volumetric flow of approximately 145 L/min (38.3 gal/min).

The coolant weight is then equal to $kQ^e w'^f$, assuming k = 10s, e=0, and f=1, the coolant weight is then 24.1 kg (53.13 lb).

Water glycol mixtures and other coolants were ruled out due to the advantage of water in both its simplicity and its potential use in recirculating the stack's water vapor exhaust for cooling and utilizing it in the air system's humidifier.

We designed the coolant tank to hold the required volume of 24.1 L (6.37 gal), which we sized proportionally to an existing 5-gallon universal aluminum tank produced by Boyd Welding [12]. This is the best available option to store our coolant as it is lightweight, durable, and capable of withstanding high temperatures and thermal cycles. Scaling accordingly, *Draco*'s coolant tank weighs 5.33 kg (11.75 lb), and its dimensions are 330.2 x 220.3 x 330.2 mm (13 x 8.67 x 13 in.).

5.3.3 Radiator Fan

We then sized the radiator fan according to the convective cooling airflow rate, which is calculated using conservation of mass at an air speed of 10 m/s. This results in an air flow rate of 1.03 kg/s at 0.914 m^3/s (2.27 lb/s at 32.27 ft^3/s).

We selected the SPAL VA113-BBL504P/R/A/N-94A brushless axial fan accordingly [13]. This model is capable of providing airflow up to 1.18 m^3/s (41.67 ft^3/s) and is the lowest weight, highest efficiency, and most reliable readily available fan we found [13]. Other components either had AC power inputs, were unable to throttle, or were made of plastic, which may fail under the high-temperature conditions, so this model is the best for *Draco*'s usage.

5.3.4 Coolant Pump

For our coolant pump, we selected the SPAL C01-BBL531P/P-G01 brushless pump [14] because it is capable of handling up to 200 L/min (52.83 gal/min) in a lightweight package of only 2.76 kg (6.08 lb), and a maximum power consumption of only 650 W (0.87 hp). This was the most lightweight, highest efficiency, and reliable pump for the flow rates required by our cooling system, and is therefore the most optimal selection.

5.3.5 Coolant System Summary

The remaining cooling system components, the filter, regulator, and power allocation, are each approximately 1% of the total cooling system weight, so the total cooling system weight is 41.84 kg (92.24 lb).

5.4 Air System Design

5.4.1 Blower Sizing

The air system is sized at maximum power. The volumetric airflow required to sustain a power output of 196.58 kW is approximately 0.39 m^3/s (13.73 ft^3/s).

(a) Radiator (b) Coolant Tank (c) Radiator Fan (d) Coolant Pump

Figure 5.3: Cooling System Components

The blower must be able to maintain this flow rate, run on DC directly from the stack without an inverter, and throttle flow in small increments. We found that the Rotron CENTRIMIL centrifugal blower is the lightest and lowest power option on the market that meets these requirements [15]. It requires an input of only 876 W (1.175 hp) at 27.5 V DC and only weighs 4.97 kg (10.96 lb). This component is perfectly sized for our application, highly reliable, and proven for use in aerospace applications.

5.4.2 Humidifier Sizing

The Fumatech Ecomate H100N humidifier meets *Draco*'s requirements for stack efficiency [16]. In the loiter segment of the mission, the airflow rate is 94.8 g/s (0.21 lb/s) or 5688 L/min (1502.6 gal/min). Scaling this model, rated at 5000 LPM (1320.9 gal/s), our humidifier design is 7.05 kg (15.54 lb), and measures 205 x 358 x 325 mm (8.07 x 14.09 x 12.80 in).

5.4.3 Deionizer

The humidifier needs water vapor to function, so the best option is to recycle the steam emitted by our fuel cell. By recycling the stored water, we ensure that *Draco* has minimal shift in center of gravity over the course of its mission. However, because the steam emissions may contain ions that could damage the fuel cell, we must include a deionizer in *Draco*'s design. We found that the Mann+Hummel IonFree Generation Ion exchange filter meets *Draco*'s needs for vapor recirculation, while ensuring reliability and preventing electrical shorts in our fuel cell stack. The high capacity model weighs only 1.1 kg (2.43 lb) and is optimal for *Draco*'s demands of water vapor output and airflow rates [17].

5.4.4 Airflow Sensor

To ensure accurate and autonomous throttling of air based on power draw, we included the Bronkhorst IN-FLOW F-106DI airflow sensor for our PEMFC system [18]. This model's exceptionally wide measurement range easily encompasses *Draco*'s maximum airflow requirement and fits the needs of the mission. Its robust IP65-rated industrial design, digital communication capabilities, and high precision make it well-suited for reliable, real-time airflow monitoring in demanding aerospace environments. It weighs 9.5 kg (20.9 lb) and requires a low input of 1.5 W (0.002 hp) and 24 V.

Other components, the filter and regulator, are approximately 1% of the total air system weight, so the total system weighs 22.62 kg (48.94 lb).

5.5 Hydrogen Storage and Supply System

The hydrogen supply system for our PEMFC is designed as a passive, pressure-regulated system to ensure reliable and efficient fuel delivery with minimal complexity. Hydrogen is supplied from a high-pressure storage tank and reduced in two stages: first by a high-pressure regulator to a safe intermediate pressure, and then by a low-pressure regulator to the operating pressure of the fuel cell stack. Since our stack operates at an

(a) Blower (b) Humidifier (c) Deionizer (d) Airflow Sensor

Figure 5.4: Air System Components

absolute pressure of 1 atm on the cathode side, the low-pressure regulator is set to maintain the hydrogen supply at approximately 1.2 atm of absolute pressure. This slight overpressure ensures a consistent pressure differential across the membrane, which supports steady hydrogen diffusion into the anode channels and prevents oxygen or nitrogen crossover from the cathode.

Importantly, the system does not require active hydrogen throttling or mass flow control, as hydrogen consumption passively adjusts according to stack current draw based on Faraday's Law. This passive approach is widely adopted in lightweight fuel cell systems such as UAVs and small-scale mobile power applications because of its simplicity, low parasitic load, and high reliability. We further ensure safety by including pressure relief valves on both the high- and low-pressure sides of the system, avoiding overpressure. Overall, this configuration provides a robust and efficient hydrogen delivery solution that aligns with the performance requirements and operational profile of our fuel cell system.

Draco contains two Type 4 cylindrical hydrogen tanks manufactured by ILJIN Hysolus [19]. Each tank holds 185L (48.87gal) and are rated at the maximum allowable pressure of 700 bar (10.15 ksi) set by the RFP. The total hydrogen stored is 14.8 kg (32.63 lb), and the total empty weight for the two tanks is 175 kg (385.81 lb).

Each tank uses the TESCOM Series HV-7000 Onboard Regulator as the high pressure regulator, which steps the pressure down from 700 bar (10.15 ksi) to 30 bar (435.11 psi), and weighs 1.6 kg (3.5 lb) [20]. Then, the Pressure Tech LW351 Pressure Regulator drops this pressure down to 1.2 atm and weighs 0.2 kg (0.44 lb) [21].

Each high-pressure relief valve, the Goetze Series 492, weighs 1.4 kg (3.1 lb), and each low-pressure Type 946 Threaded Safety Relief Valve by Seetru Limited weighs 1 kg (2.2 lb) [22, 23]. With 2 tanks, and one of each relief valve per tank, the hydrogen storage and supply system weighs 183.4 kg (404.33 lb), with 14.8 kg (32.63 lb) of hydrogen stored.

5.6 Electrical System Design

Draco uses the Aradex VP5000 to step up voltage from both the 400V PEMFC stack and battery to the higher voltage needed by the electric motors. It is a reliable DC-DC converter that supports dual inputs and offers the power capacity and high efficiency needed for this application [24].

To optimize system performance and ensure operational reliability, we integrated a buffer battery into *Draco*'s power system alongside the PEMFC. This battery provides the extra power needed for the hover and vertical climb mission segments. By subsidizing power spikes, the buffer battery reduces the peak power demands on the fuel cell, allowing for a smaller, lighter stack and balance-of-plant components, significantly lowering overall system mass.

Our initial design, relying solely on a fuel cell system sized to meet peak power independently, resulted in a projected net system mass of approximately 250 kg. With the incorporation of the buffer battery, our

(a) Hydrogen Tank (b) High Pressure Regulator (c) Low Pressure Regulator (d) Airflow Sensor (e) Low Pressure Relief Valve

Figure 5.5: Hydrogen Storage and Supply System Components

current hybrid system has a net mass of 231.56 kg, reflecting a notable 7.4% mass reduction of 18.44 kg (40.65 lb). This weight reduction was essential to align with aerodynamic sizing constraints. A higher system mass would have required greater lift, leading to higher power demands, a larger fuel cell stack, and further weight increases.

Additionally, the buffer battery provides a critical safety advantage. In the event of a complete fuel cell system failure, the battery alone is capable of supplying enough energy to support loiter and a safe landing, acting as an emergency backup power source. This redundancy enhances the overall fault tolerance of the system, which is especially important given our use of PEM fuel cells, a relatively new and unproven technology in flight applications where safety is a primary concern.

To meet our design constraint of a maximum 30 kg battery system, with 5 kg allocated to casing and structural components, we evaluated battery cell options based on performance at a net 25 kg cell mass. Given our emphasis on supporting high-power segments rather than long-duration endurance, we prioritized gravimetric power density over energy density.

Among the options considered, the Samsung 40T and Tesla Model 3 21700 cells were evaluated for down-selection. While the Tesla cell offered a slightly higher gravimetric energy density (253 Wh/kg vs. 205.71 Wh/kg), the Samsung 40T provided significantly greater gravimetric power density (2314.29 W/kg vs. 1138.51 W/kg) [6]. When scaled to 25 kg, the Samsung 40T configuration delivers a peak power output of 57.86 kW and an energy capacity of 5.143 kWh, well-suited for supplementing the fuel cell during high-power phases. In contrast, the Tesla configuration, though offering 6.325 kWh of energy, only delivered 28.46 kW of peak power within the same mass constraint. Given its superior power density and ability to reduce the fuel cell system size while adding a vital layer of safety, the Samsung 40T was selected as the optimal battery for our hybrid power system.

Fuel Cell Control Unit (FCCU): The FCCU is the primary controller for operation of the PEMFC system, and ensures reliable operation by both monitoring and regulating the stack, air supply, cooling loop, hydrogen storage, and electrical subsystems [25]. A closed-loop control algorithm processes real-time system feedback and pilot collective input to maintain optimal performance under varying load conditions. The estimated weight of the FCCU is 6.72 kg, scaled proportionally to the system's maximum stack current, following the methodology outlined in Datta (2021) [8].

5.7 PEMFC Stack System Summary

The PEMFC system weighs 430.18 kg (948.4 lb), about 30% of the vehicle weight. An itemized breakdown of system weights is shown in Table 5.2. With all of these components accounted for, we prioritize PEMFC

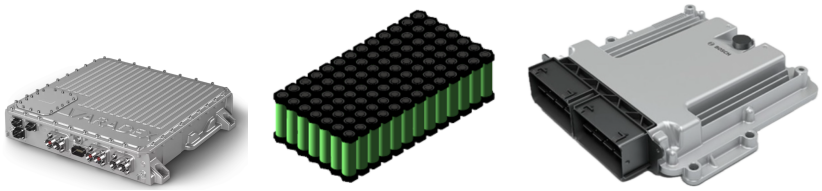

(a) Boost Converter (b) Battery (c) Fuel Cell Control Unit

Figure 5.6: Electrical System Components

system integration in our airframe design and volume allocation, discussed in Section 8.

Table 5.2: PEMFC Stack System Weight Breakdown

System Component	Weight	
	kg	lb
PEMFC Stack	**100.8**	**222.23**
Air System	**22.62**	**49.87**
Humidifier	7.05	15.54
Mass Flow Meter	9.5	20.94
Blower	4.97	10.96
Deionizer	1.1	2.43
High-Temperature Cooling System	**41.84**	**92.24**
Radiator	5.93	13.07
Coolant	24.1	53.13
Fan	2.5	5.51
Tank	5.33	9.55
Pump	2.76	6.08
Filter	0.41	0.90
Regulator	0.41	0.90
Power	0.41	0.90
Electrical	**66.72**	**147.09**
Controller	6.72	14.82
Battery (with casing)	30	66.14
DC/DC Converter	30	66.14
Hydrogen Supply System	**183.4**	**404.33**
Tanks	175	385.8
Pressure regulators	3.6	7.94
Pressure relief valves	2.4	5.3
Fuel	**14.8**	**31.3**
Total	**430.18**	**948.4**

6 Propulsion and Transmission

Draco's power for the drivetrain comes from the PEM Fuel Cells in the form of direct electrical current running at 610 VDC after boost converters to power the two EMRAX 348 electric axial flux motors [26]. This power is transferred to the main and tail rotors using a mechanical drivetrain consisting of shafts and two gearboxes for the main and tail rotors. The design process was centered on weight reduction and simplification of the drivetrain architecture. The model of our final design of the main transmission is shown in Figure 6.1.

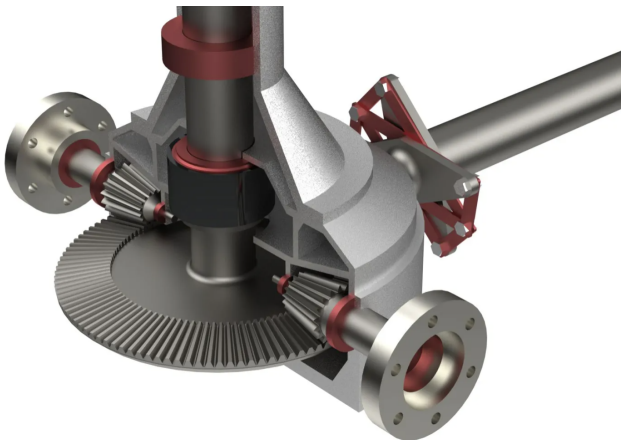

Figure 6.1: *Draco*'s Transmission Rendering

6.1 Transmission System Overview

Draco uses a 2-speed drivetrain to allow for more efficient power usage in specific mission segments, extending its loiter endurance.

The two operational speeds are referred to as the High Power Configuration (**HPC**) and Low Power Configuration (**LPC**). The HPC is used for mission segments such as hover and vertical climbs, where high power is required. The LPC is used in loiter and cruise, where low power is required.

6.1.1 High Power Configuration

For the HPC, the two independent EMRAX 348 electric axial flux motors are operating at 262.8 rad/s (2500 RPM). Both motors feed into a large center bevel gear with a sprag clutch built into the motor drive shaft to allow the other motor to drive the rotor still if one motor fails. The motor pinion and main gear reduce the motor rotational speed down to 40.8 rad/s (390 RPM) and transmit to the main rotor through a subcritical shaft. On the main gear, another bevel gear is tapped to provide power to the tail drive shaft. The tail drive shaft bevel gear returns the rotational speed to 262.8 rad/s (2500 RPM), being transferred by a supercritical two-segment drive shaft operating between the shaft's first and second natural frequencies. It is then fed into the tail gearbox, increasing the rotational speed to 284.5 rad/s (2717 RPM).

6.1.2 Low Power Configuration

For the LPC, the transmission scheme is the same, but the speeds are only 66% of HPC. So the EMRAX 348 motors run at 172.8 rad/s (1650 RPM), reducing to 26.9 rad/s (257 RPM) for the main rotor. As was the case in HPC, the tail drive shaft operates at the same rotational speed as the motors, and then the tail rotor operates at 187.8 rad/s (1793 RPM).

These reductions are possible with the offloading of power to the wings for the lift component. Also, while in loiter, the power for the tail is reduced by 40% of its HPC or just 4% of the total installed power.

6.2 Motor Selection

Electric motors come in two main categories: axial and radial flux. The radial flux motors were ruled out due to their weaker power density than axial flux motors. Thus, the weight and volume allocation can be reduced with the use of axial flux. For axial flux, the two motors selected for comparison were the EMRAX 348 from EMRAX E-Motors and the D500 from EvoLite, summarized in Table 6.1 [26].

Unfortunately, the D500 needs longer peak power than just 30 seconds for our design.[27] Also, the operating speed to supply the correct power would require about 366.5 rad/s (3500 RPM) leading to more complex heavier multi-stage reductions for correct rotor rotational speeds, and while it outputs more energy per

Table 6.1: Electric Motor Selection

	EMRAX 348	D500
Mass [kg (lb)]	43.9 (96.8)	30 (66.1)
Peak Power [kW (hp)]	400 (536), 2 minutes	350 (469), 30 seconds
Approximate Volume [m^3 (ft^3)]	0.0105 (0.369)	0.141 (0.50)
Power Density [kW/kg (hp/lb)]	9.1 (5.535)	11.6 (7.056)

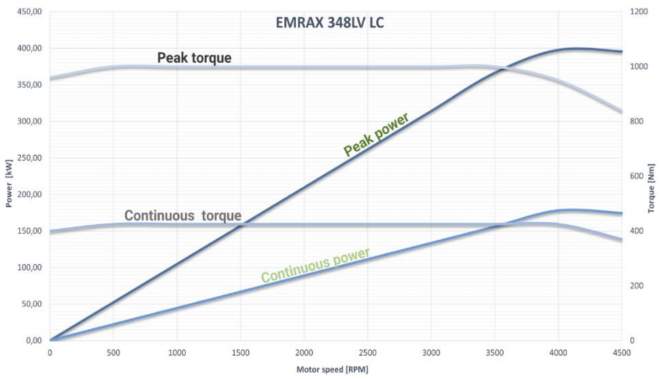

(a) EMRAX 348: Torque and Power map

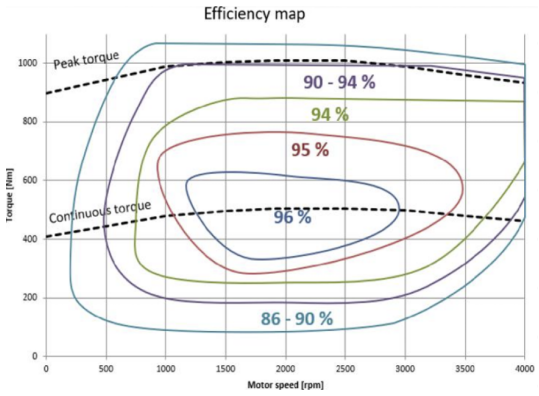

(b) EMRAX 348: Torque vs. RPM with Efficiency

Figure 6.2: EMRAX 348 Performance Specs

unit mass, it takes more energy to run at 800VDC [27] compared to the EMRAX 348 running at 610VDC. This would lead to a decrease in loiter time, so we chose EMRAX 348 as the superior option for *Draco*. Its performance, including power, torque, and efficiency with respect to rotational speed, is shown in Figure 6.2.

6.3 Gearbox Design

The two gearboxes that Draco utilizes are the main gearbox and the tail gearbox. The main gearbox is a bevel gear with two pinion inputs from the motors and one pinion output to the tail. The tail gearbox is a simple bevel pinion gear that changes the direction of rotation and speed of the tail rotor.

6.3.1 Main Gearbox Design

By keeping the motor rotational speed low, Draco is able to use a single reduction stage accomplished by a bevel gear. The steel to be used is Ferrium C64. This was selected because of its consistency for the S-N curve between room temperature and high temperatures.[28]

It was also verified to have an endurance bending fatigue strength above the bending stresses that the pinion would experience [29]. This bending stress was initially designed for fatigue at the highest power events, resulting in a heavy gearset. But through the use of a modified Miner-Palmgren Rule analysis [30] using the Lewis bending stress [29], it was found that we could design for a much lower power since the high power events are very low in cycles compared to those of the low power events, such as loiter. This, in effect, lowered the mass of the gearset considerably while remaining in an infinite life range of service.

Since the bevel gears use the involute design, the minimum number of teeth on the pinion recommended by KHK Gears [31] is 17 teeth with a 20° pressure angle. With the architecture of this design being a single reduction, the gear will need 109 teeth to reduce the rotational speed to what our main rotor needs. This is summarized in Table 6.2.

The housing was designed with the transfer of loads in mind, along with weight reduction. The housings are made from a die-cast of Magnesium Alloy ZK61A-T5, with its low density compared to similar Aluminum Alloys. We compared it with A380.0-F Aluminum Alloy to select a material. As shown in Table 6.3, the two

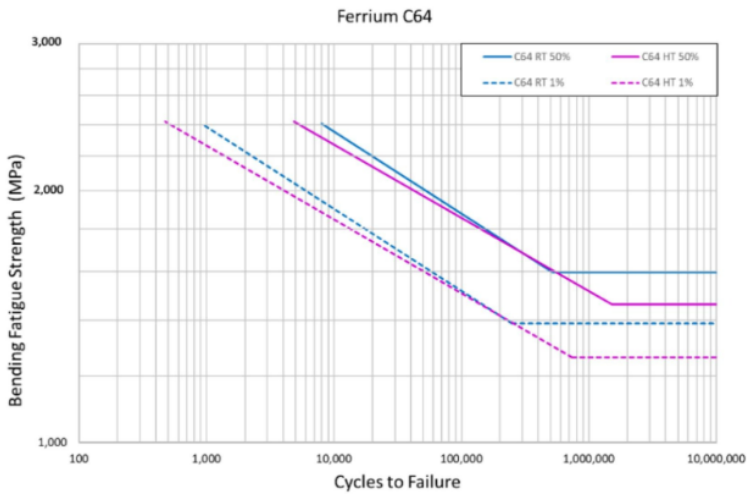

Figure 6.3: Ferrium C64 Stress-Strain Curve

Table 6.2: Main Gearbox Pinion and Gear Specs

	Pinions	Gear
Shaft angle [°]	90	90
Pressure angle [°]	20	20
Number of Teeth	17	109
Cone Distance [mm (in)]	155.67 (6.13)	155.67 (6.13)
Diametral Pitch [teeth/cm (teeth/in)]	3.54 (9)	3.54 (9)
Face Width [mm (in)]	28.22 (1.11)	28.22 (1.11)
Pitch Diameter [mm (in)]	47.98 (1.89)	307.62 (12.11)
Addendum [mm (in)]	2.82 (0.11)	2.82 (0.11)
Dedendum [mm (in)]	3.53 (0.14)	3.53 (0.14)

are comparable in strength, but the Magnesium is about 38.4% lighter than the A380.0-F Aluminum Alloy and thus is the best choice.

Table 6.3: Main Gearbox Housing Material Comparison

	ZK61A-T5 (Mg)	A380.0-F (Al)	% Difference
Density [g/cm^3 (oz/in^3)]	1.87 (1.08)	2.76 (1.60)	+38.4%
Ultimate Tensile Strength [MPa (ksi)]	310 (44.96)	324 (46.99)	+4.4%
Yield Tensile Strength [MPa (ksi)]	185 (26.83)	159 (23.06)	+15.1%
Shear Strength [MPa (ksi)]	170 (24.66)	185 (26.83)	+8.5%

The rotor drive shaft connected to the main large gear has an axial load due to the thrust, and this is offloaded from the gear system by a conical bearing pair that is spaced out to help the offloading of remaining bending moments after the static mast.

6.3.2 Tail Gearbox Design

The tail gearbox is a simple 90° bevel gearbox with an increase in rotational speed. This transmission design does not include any belt drives that would focus on a specific decimal rotational speed multiplier and instead must use fractional multipliers. Hence, Draco's tail gearbox goes over the minimum requirement of 17 teeth as stated before. The tail gearbox needed an input of 25 teeth to an output of 23 teeth to increase the 262.8 rad/s (2500 RPM) to 284.5 rad/s (2717 RPM). Exact dimensions of the tail gearbox are summarized in Table 6.4.

Table 6.4: Tail Gearbox Gear Specs

	Input Gear	Output Gear
Shaft angle [°]	90	90
Pressure angle [°]	20	20
Number of Teeth	25	23
Cone Distance [mm (in)]	47.94 (1.89)	47.94 (1.89)
Diametral Pitch [teeth/cm (teeth/in)]	3.54 (9)	3.54 (9)
Face Width [mm (in)]	15.97 (0.63)	15.97 (0.63)
Pitch Diameter [mm (in)]	70.56 (2.78)	64.91 (2.56)
Addendum [mm (in)]	2.82 (0.11)	2.82 (0.11)
Dedendum [mm (in)]	3.53 (0.14)	3.53 (0.14)

The housing for the tail gearbox is also made of Magnesium ZK61A-T5, like the main gearbox.

6.4 Shaft Design

There are two main shafts involved in the transmission for *Draco*. These are a subcritical main rotor drive shaft and a two-segment supercritical tail drive shaft.

6.4.1 Tail Drive Shafts

For the tail drive shaft, three configurations and three materials were considered, totaling nine cases to choose from. The three configurations were a four-segment subcritical shaft, a two-segment supercritical shaft between the first and second natural frequencies, and finally a single-segment supercritical shaft between the second and third natural frequencies. The three materials considered were Steel 15-5 PH, Aluminum 2024 Alloy, and Titanium TA-6V.

The diameter and thickness dimensions were found by calculating the lowest possible mass after finding all possible solutions for each case based on several criteria. We tested outer diameters ranging from 1 mm to 100 mm, and the thickness ranged from 1 mm to 5 mm. The criteria are shown below:

- Frequency: Setting the operating rotational speed of the tail drive shaft to our design of 262.8 rad/s (2500 RPM) and then allowing a variance of 110% above and 80% below, then pushing out these limits by 13%, making a lower and upper margin of error.
  - Subcritical: Finding all outer diameter and thickness combinations that result in a shaft with the upper margin of error speed below the first natural frequency.
  - Supercritical 1 to 2: Finding all outer diameter and thickness combinations that result in a shaft with the upper and lower margins of error speeds below the second and above the first natural frequency.
  - Supercritical 2 to 3: Finding all outer diameter and thickness combinations that result in a shaft with the upper and lower margins of error speeds below the third and above the second natural frequency.
- Resistance: This was set by using a Von Mises shear stress analysis to find the minimum thickness for each outer diameter, assuming pure torsional stresses with a safety factor of 1.5 on the stress[32].
- Strain: This was set by limiting the angle of twist in the shaft. The minimum thickness was found using the limit of 0.7°/m [32].
- Fatigue: This was set by using the Goodman Mean Stress Analysis for both high and low cycles with a safety factor of 2. This was also finding the minimum thickness for each outer diameter [32].

We selected the Aluminum 2024 Alloy running at supercritical between the first and second natural frequencies. While the Aluminum has low strength values compared to the other options, the increased dimensions compensated for this, and due to its relatively low density, it was still lighter overall than the other 8 op-

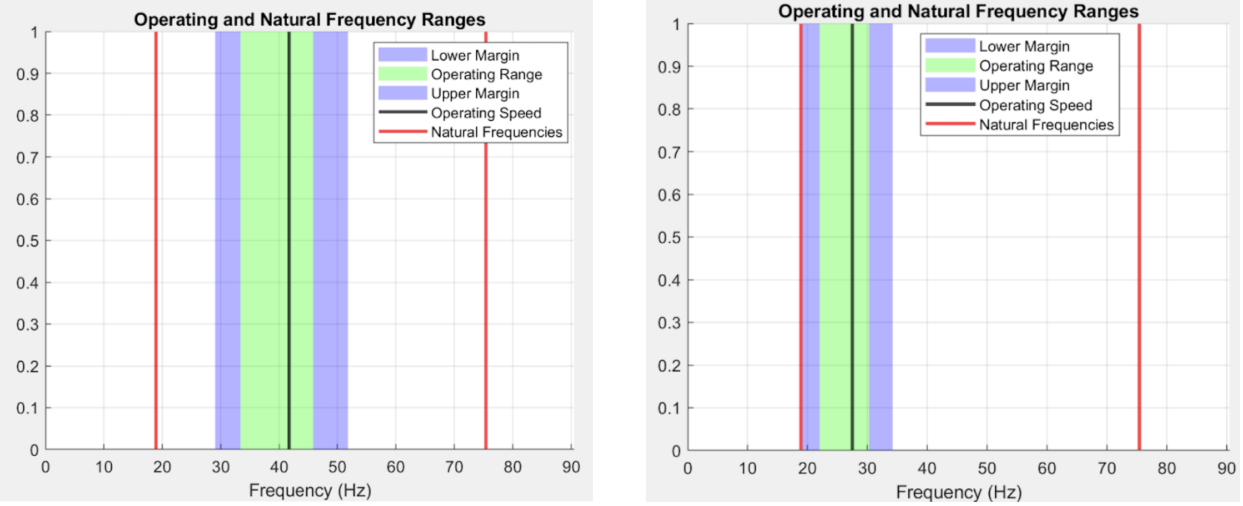

(a) High Power Configuration

(b) Low Power Configuration

Figure 6.4: Operating and Natural Frequencies at Operating Shaft Speeds

tions, which are summarized in Table 6.5. The numbers are organized as DD / TT / MMM / X: DD = Outer Diameter [mm], TT = Thickness [mm], MMM = Mass [kg], X = Number of additional bearing and dampeners needed.

The supercritical shaft is also self-stabilizing, so this choice improves the shaft stability overall [33].

Table 6.5: Tail Drive Shaft: Weight Trade Study

	Supercritical 2 to 3	Supercritical 1 to 2	Subcritical
Steel 15-5 PH	74 / 2.5 / 25.4 / 0	45 / 1.5 / 9.76 / 1	45 / 1.5 / 10.7 / 3
Aluminum 2024 Alloy	73 / 2.5 / 8.67 / 0	58 / 2.0 / 6.13 / 1	58 / 2.0 / 7.36 / 3
Titanium TA6V	74 / 2.5 / 14.3 / 0	50 / 2.0 / 8.24 / 1	50 / 2.0 / 9.32 / 3

Index: DD / TT / MMM / X: DD = Outer Diameter [mm], TT = Thickness [mm], MMM = Mass [kg], X = Number of additional bearing and dampeners needed

Variable Speeds

Because the tail drive shaft operates between the first and second natural frequencies, there is a possibility of entering resonance when reducing the rotational speed. To alleviate this, we confirmed that the first natural frequency does not enter the lower margin of error of 13% during the Low Power Configuration (LPC), as illustrated in Figure 6.4.

Damping

Two damping devices will be placed at the center of each shaft segment to ensure safe transit over the first natural frequency. The damping material used is Torlon PAI 5030, one of the two Torlon products FAA-approved for civil use [31]. At the locations of these dampeners, the shaft will have a coating of additional aluminum 2024 to reduce wear over the shaft's life.

Other considerations for transferring power to the tail rotor were to place a small electric motor at the end of the tail boom, running directly into the tail rotor. Still, even using the smallest EMRAX motor, the EMRAX 188, with a mass of 7.9kg, then to include the wiring and coolant from the main body, and an extra motor controller, it was heavier than the standard shafting architecture with more.

6.4.2 Main Rotor Shaft

The main rotor shaft was found by almost the same process as the tail shaft, with a few additions. It was set to be a subcritical shaft due to its lower rotational speed and shorter length compared to the tail rotor

shaft, and the main rotor shaft had extra requirements imposed on it, like needing to support the axial loads of the main rotor thrust and the bending moments of the rotor. The static mast bearing locations were also selected to reduce these bending moments within the shaft and decrease the size and mass of the shaft.

The final design of our transmission is visualized and labeled in Figure 6.5.

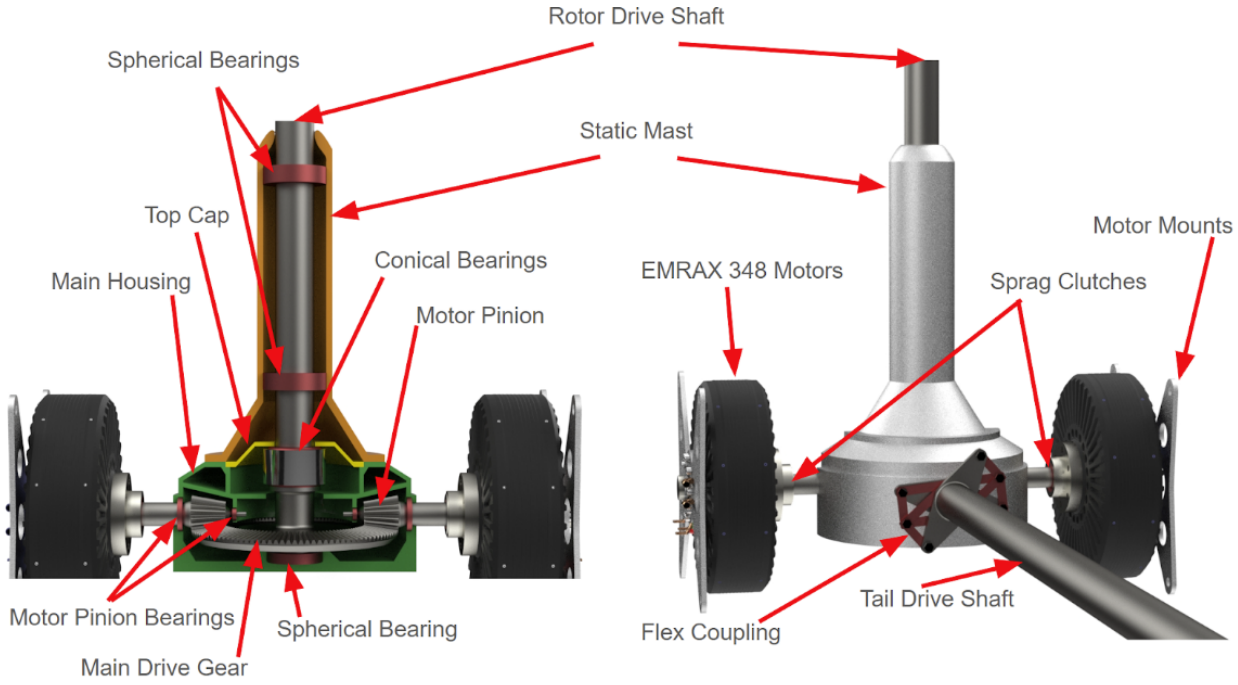

Figure 6.5: Main Transmission Layout, Front View (left) and Back View (right)

7 Rotor Hub and Blade Structural Design

7.1 Blade Internal Structure

The internal structure of the main rotor blade is shown in Figure 7.1. In flight, the D-spar is the primary load carrier and will provide torsional stiffness while also having a simple geometry for manufacturing. Rohacell 31 foam will fill the inside of the D-spar and a majority of the blade's volume. Rohacell 31 is a lightweight, rigid, and cheap material with a closed-cell composition, containing no chlorofluorocarbons (CFCs), minimizing environmental impact. In addition, a steel leading edge weight is placed near the leading edge inside the D-spar to maintain the center of gravity at the elastic axis and quarter chord. The blade is covered in a $\pm 45^{\circ}$ graphite/epoxy skin to provide a majority of the torsional stiffness of the blade. A copper mesh will provide protection against lightning strikes in rough weather conditions. The stainless steel leading edge protection will prevent erosion and corrosion from particulates that may come in contact with the blade in flight.

7.2 Main Rotor Hub

7.2.1 Hub Configuration Selection

Based on our design philosophy of utilizing proven, safe helicopter design concepts, we considered five common types of hub configurations for our main rotor, including the following:

- **Teetering hubs** are compatible with only two-bladed designs, with a single teetering in which blades are able to flap, allowing for the simplest design. They also require little maintenance.

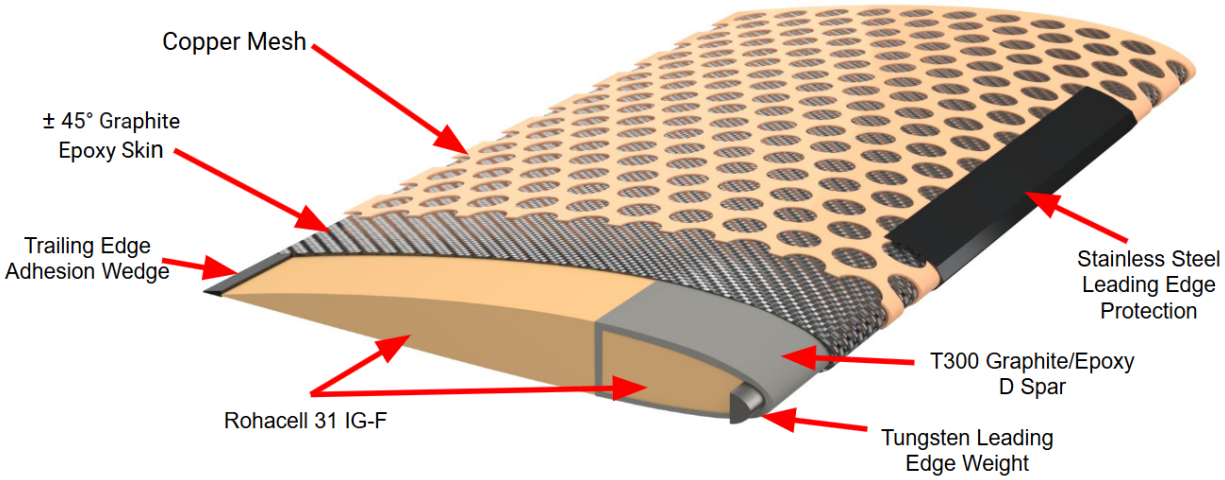

Figure 7.1: Cross-Section of Main Rotor Blade

- **Articulated hubs** consist of mechanical hinges in the pitch, flap, and lagging axes. They also allow for smoother operation and lower vibrations, which are important for passenger comfort.
- **Semi-Articulated hubs** use elastomeric bearings and lead-lag dampers to teeter and feather. They are also mechanically compact and reduce the amount of maintenance that is needed.
- **Hingeless hubs** require a bearing for pitch control. In addition, they also need flexures for flap and lag. They are relatively compact and contribute less to drag in forward flight.
- **Bearingless hubs** are rigid, without bearings or hinges, allowing for flexibility in the blade and absorption of lead-lag, flapping, and feathering forces. However, advanced materials require a more expensive production, driving up costs.

Considering these factors, the articulated rotor with spherical elastomeric bearings was chosen for *Draco*'s design. It provides low maintenance operation and clear visual cues of wear and tear to prevent future failure. Articulated hubs are less complex than semi-articulated and hingeless designs and are more affordable relative to bearingless hubs.

7.3 Main Rotor Hub Assembly

Draco's main rotor hub is based on the proven design of the Guimbal Cabri, and it is shown in Figure 7.2. The major components are the flex plate, blade grip, pitch horn, pitch links, scissor links, swashplate, spherical elastomeric bearings, elastomeric dampers, and swashplates. Titanium-8Al-1Mo-1V alloy was selected for the hub yoke and pitch casings due to its high strength-to-weight ratio, fatigue life, and resistance to corrosion. Other materials such as steel and aluminum were considered, but they are either too heavy or lack the strength required, respectively.

7.4 Swashplates

Considering reliability and safety, *Draco* utilizes a conventional swashplate mechanism, rather than experimenting with new and novel ideas. The swashplate design is also shown in Figure 7.2. The bearing between the rotating and non-rotating swashplate is placed in a low-friction sleeve that allows for the mechanism to have collective and cyclic control. Inputs from the pilot are translated to three symmetrical linear actuators that are transmitted to the swashplates.

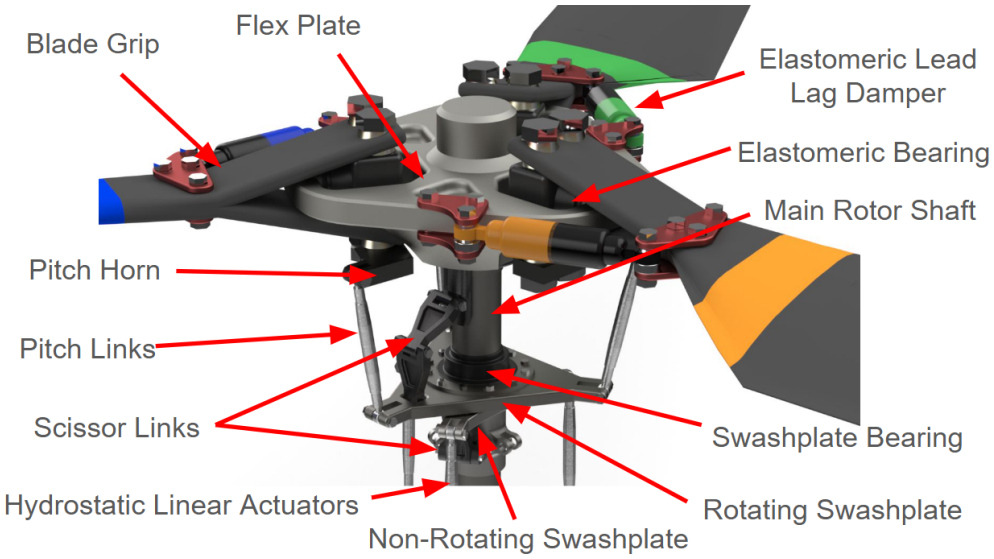

Figure 7.2: Main Rotor Hub

7.5 Tail Rotor Hub Design

Draco has a two-bladed teetering tail rotor consisting of similar components and composite materials for the blade as the main rotor. A teetering hub was chosen due to its mechanical simplicity and proven reliability. A mast bump stopper is placed within the yoke to prevent any damage that may be caused from mast striking. A low-profile hub cap is also placed on the rotor to reduce drag in forward flight. A $\delta 3$ coupling of 45° is part of the tail rotor to minimize blade pitch-flapping without increasing the load on the hub. This also reduces the maximum blade flapping angles, therefore reducing potential mast bumping or fuselage strikes from the blades. We implemented a clearance angle of 12°. The final design is modeled in Figure 7.3.

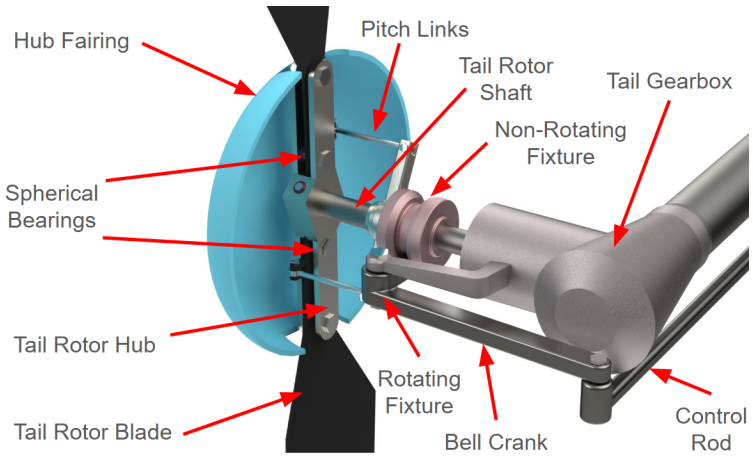

Figure 7.3: Tail Rotor Hub

7.6 Tail Rotor Blade

The tail rotor uses the OA-212 airfoil and has a diameter of 1.406 m (4.61 ft) and a uniform chord of 12.9 cm (5.1 in). With a lever arm of 5.8 m (19 ft) from the center of gravity (C.G.), the tail rotor provides sufficient antitorque thrust in hover and cross winds. The tip clearance between the main rotor and tail

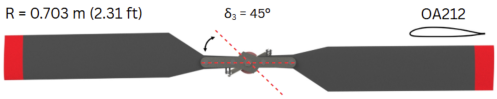

Figure 7.4: Tail Rotor Blade Geometry

rotor well exceeds the minimum allowable clearance of 0.12 m (0.4 ft). Additionally, the tail rotor blades are positioned 0.154 m (0.505 ft) from the tail boom to prevent blade strikes, accounting for a rotor flapping angle of 12° and a tail boom angle of 0.61°. A side-view of the tail rotor is shown in Figure 7.4.

8 Airframe Design

8.1 Airframe Structure

Draco's airframe is designed for safety, aerodynamic efficiency, and minimal volume and weight, which are critical due to the substantial mass of the onboard hydrogen plant components. The semimonocoque structure was chosen to optimize the strength-to-weight ratio with efficient load distribution. This configuration enables us to create a structurally sound aircraft that remains lightweight and compact enough to make hydrogen propulsion feasible. The airframe structure consists of three primary segments: the fuselage, the wing, and the tail and empennage. Figure 8.1 shows isometric views of the vehicle's full internal rendering and its skeletal structure with all functional components hidden.

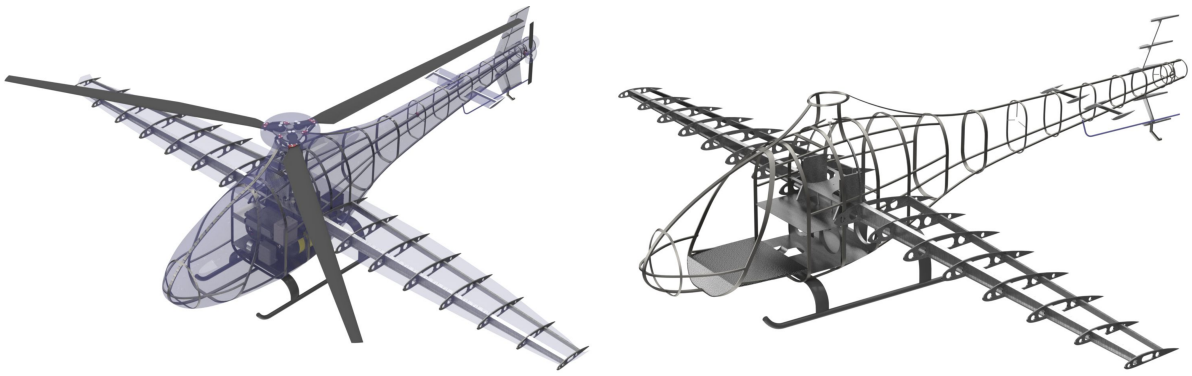

(a) Full Internal View (b) Skeletal Structure

Figure 8.1: *Draco*'s Full Airframe

8.2 Volume Allocation

To meet cabin requirements, the internal space provides a minimum of 1.25 m (4.1 ft) in width, 1.5 m (4.92 ft) in length, and 1.45 m (4.76 ft) in height. Internal components were arranged to maintain a minimal frontal area, closely matching the front-facing area of the cabin, 1.25 m × 1.45 m (4.1 ft x 4.76 ft). This configuration minimizes overall aircraft volume while maximizing aerodynamic efficiency. Given the fixed total aircraft length driven by the dimensions of the main and tail rotors, this compact packaging also helps reduce total structural weight. The organization of internal components and the associated center of gravity are visualized in Figure 8.2. The components are positioned such that the center of gravity is directly in line with the longitudinal position of the main shaft. More details on the center of gravity analysis are included in Section 11: Weight and Balance.

8.2.1 PEMFC System Integration

Per RFP requirements, the physical integration of the PEMFC system was a major driver in our airframe geometry design. A view with only the PEMFC highlighted, and the transmission as a reference point, is shown in Figure 8.3. Plumbing is omitted from this rendering for clarity.

The most power-demanding mission segment is the vertical climb to 60 m (196.9 ft) above MSL at ISA, so this demands the highest air flow rate. To allow for suitable air flow into the PEMFC stack, based on our blower specifications and air density at this condition, we sized *Draco*'s air inlets and exits to a cross sectional area of 0.049 m^2 (0.527 ft^2 each. Inlets and exits are forward and aft of the mast fairing to efficiently utilize freestream air flow. To decrease the drag associated with these air inlets, we reduced the size of the mast

Figure 8.2: *Draco*'s Volume Allocation

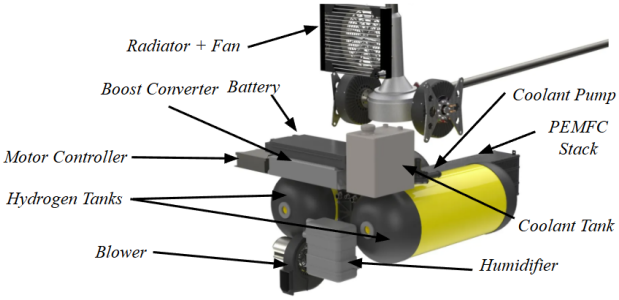

Figure 8.3: PEMFC System Integration

fairing inlets by adding additional inlets below the nose of the vehicle, for a total inlet area that meet the aforementioned needs. Inlets and exits are visualized in Figure 8.4.

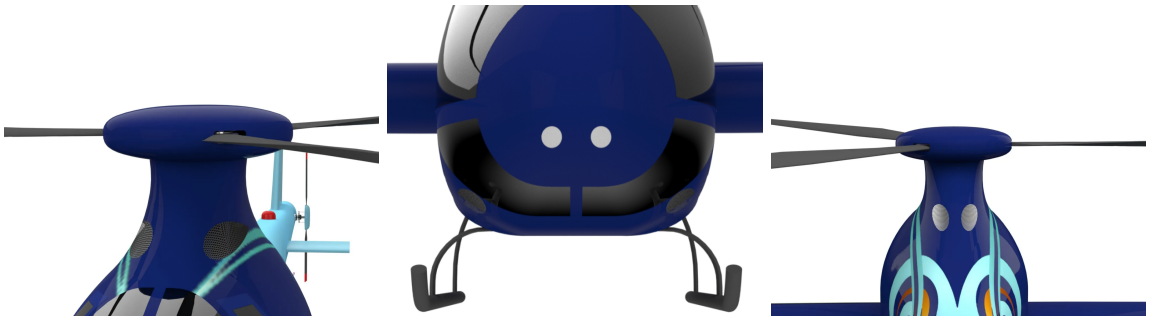

(a) Air Inlets (Mast) (b) Air Inlets (Nose) (c) Air Exhaust

Figure 8.4: Airframe Surface Locations of Air Inlets and Outlets

8.3 Fuselage

The fuselage is structured around six primary bulkheads. The first is located at the front of the windshield, and the second marks the rear of the windshield and the front edge of the cockpit doors. The third bulkhead, located at the rear of the cockpit doors, is dual-purpose. It has a thin titanium firewall to protect occupants in case of mission-critical hydrogen tank damage, and it also serves as a structural attachment point for the landing gear.

Two additional bulkheads flank the main gearbox to provide localized support. A sixth bulkhead is placed directly bolted to the second landing gear attachment beam.

The latter four bulkheads are connected by two keel beams that run along the underside of the fuselage, as well as four other longerons that span across the top and sides of the bulkheads. Longerons between the first three bulkheads are placed to border discontinuities in the skin of the fuselage. These discontinuities include structures such as the windshield, windows, and doors.

Interior components are mounted to floor structures, which transmit vertical loads into adjacent bulkheads. These floor panels are reinforced by various vertical members to support concentrated loads. A mast fairing, mounted above the fuselage, features a smooth, aerodynamic contour that transitions the surface of the fuselage into a circular opening at the main rotor hub. This fairing streamlines airflow around the protruding shaft to reduce drag. Figure 8.5 illustrates *Draco*'s skeletal structure and is color-coded for each type of support structure: red bulkheads, orange hub fairing, blue stringers and longerons, green keel beams, and yellow-green landing gear.

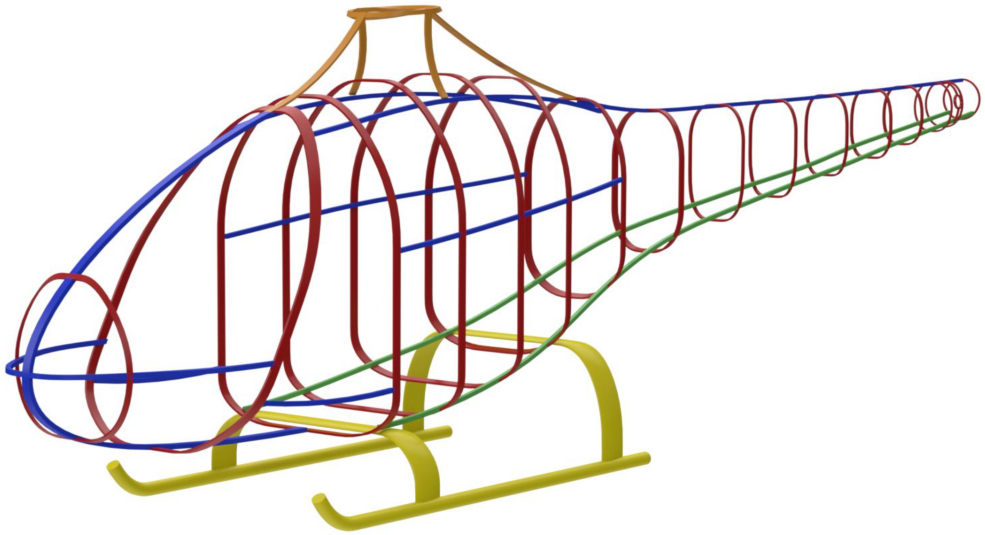

Figure 8.5: Color-Coded Fuselage Structure

The airframe structures support the entire weight of the aircraft in both compression and tension, depending on the maneuver. When in tension, the support structures are limited by the buckling failure mode more so than yielding, so we must prioritize materials with a high ratio of elastic modulus to density to simultaneously minimize mass requirements for a component of sufficient resistance to bending or buckling [34]. We used an Ashby-style material chart of elastic modulus versus density to select suitable options with high ratios of elastic modulus to density. We down-selected between 5 aluminum alloys, and decided to use Aluminum 7075 T6 because it has the highest yield strength among different alloys with similar ratios of elastic modulus to density.

8.4 Wing Structure

Two spars span from tip to tip along the wing, located equidistant from the aerodynamic center of the wing and pass directly through the fuselage to simplify structural attachments. The quarter chord is also in line with both the center of gravity and the main rotor shaft and rests above the hydrogen tanks. It is mounted to the surrounding bulkheads and floor structure to provide a continuous lift path. The primary spar through the wing's quarter chord extends the full span of the wing, while the ribs, skin, and secondary aft spar are only outside of the fuselage. This opens up internal space which can be used for functional components, primarily of the PEMFC system. This structure is shown in Figure 8.6.

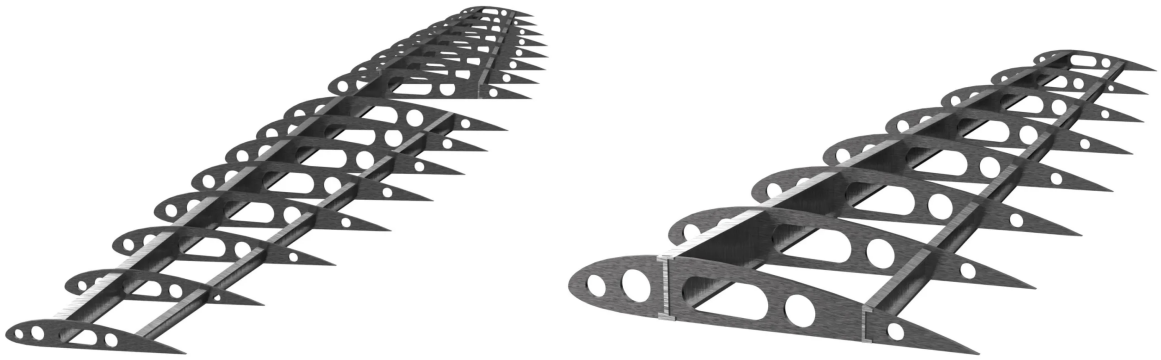

(a) Full Wingspan (b) Single Wing

Figure 8.6: Wing Internal Structure

8.5 Tail and Empennage Structure

The tail boom includes bulkheads connected by three longitudinal members: two lower keel beams and one upper longeron, continuing from the fuselage. The tail shaft is supported by a mid-span bulkhead fitted with a bearing to stabilize the shaft. The tail gearbox is positioned between two bulkheads that secure its placement and support its weight. The horizontal and vertical stabilizers have a single spar and rib on each side of the tail boom due to their relatively small size and lift. Each stabilizer spar is bolted to a bulkhead inside the tail boom.

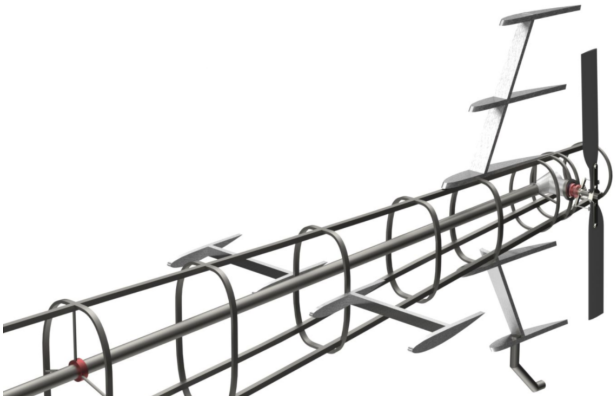

Figure 8.7: Tail Boom and Empennage Rendering

8.6 Landing Gear

Draco uses skid landing gear for its simplicity, durability, and low maintenance requirements. The landing gear has an airfoil-shaped casing for drag reduction. The skids curve upward at the front for obstacle clearance and taper down at the rear for weight savings. An 8° clearance angle from the horizontal, between the aft end of the landing gear and the lower support of the tail boom, is implemented to prevent tail striking. The landing gear is also designed to have a 34 ° rollover angle, the angle of the line connecting the C.G. and skids from the vertical.

We conducted a similar approach to material selection for the landing gear, but this time down-selected materials with high ratios of yield strength to density. Five suitable options arose, and Aluminum 7068-T6511 was selected for its high strength-to-weight ratio and cost of $4.49/kg ($2.04/lb), the most sound and affordable option of the five.

8.7 Load Paths

On the ground, loads from internal components are transmitted to the nearest bulkheads through connecting members such as floors, truss elements, stringers, and longerons. The keel beams running the length of the fuselage provide longitudinal load transfer to the landing gear, which is mounted beneath two bulkheads symmetrically positioned about the aircraft's center of gravity.

In hover, the load is concentrated at the main gearbox, which transmits the upward force of the main rotor to support the entire weight of the aircraft. The gearbox is bolted to a reinforced flooring structure that distributes loads into adjacent bulkheads. The remaining internal loads are carried by the fuselage frame, ultimately channeling to the gearbox via the interconnected keel beams and longerons. In forward flight, the wing spar, located directly beneath the gearbox, contributes lift aligned with the aircraft's center of gravity, improving aerodynamic balance and structural efficiency.

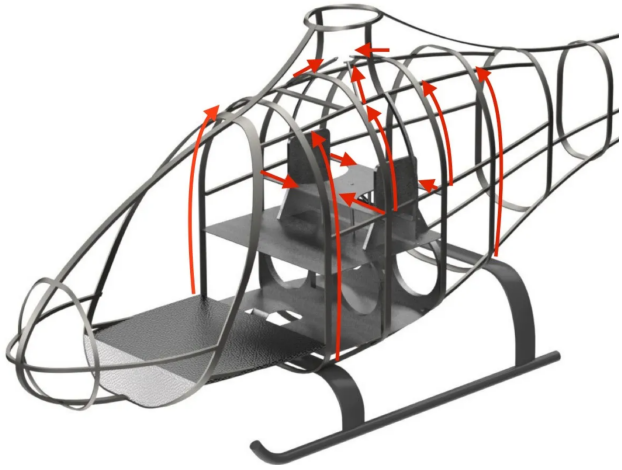

Figure 8.8: Fuselage Structure Load Paths

9 Empennage Design

9.1 Vertical Stabilizer Design

After the initial sizing of the airframe, main rotor, tail rotor, and fixed wings, a vertical tail fin was added to reduce the power requirements of the tail rotor while maintaining yaw stability, counteracting the torque of the main rotor. The benefit of offloading the tail rotor in forward flight outweighs the penalties of added weight and drag because this increases *Draco*'s endurance in loiter by reducing its rate of fuel consumption. To fully offload the tail rotor, the vertical fin would need to provide a starboard direction thrust in the form of lift of the vertical fin. The main variables to control were the airfoil shape, angle of attack against the freestream wind, and planform area. *Draco* implements a cambered airfoil, NACA 4412, to increase the lift produced at low angles of attack and surface area thus reducing the overall mass of the vertical fin and mitigating the penalty of increased drag.

Increasing the angle of attack reduces the needed surface area, but too drastic an increase could lead to stalling in high yaw conditions, so this design has an upper limit of 5° angle of attack. With this, along with the best endurance flight speed during loiter, a surface area of 0.82 m^2 is necessary. However, this is assuming uniform freestream airflow, which is not the case due to the main rotor wake in forward flight. Therefore, an assumed 70% of the uniform flow dynamic pressure was used to determine a new surface area requirement of 1.18 m^2 [35].

This design allows *Draco* to reduce power of the tail rotor from 10% of the main rotor power to only 4%, leading to an increase of endurance in the loiter segment of the mission by 10 minutes. This 4% power requirement is to overcome the drag of the rotating blades and transmission loss in the tail rotor. The

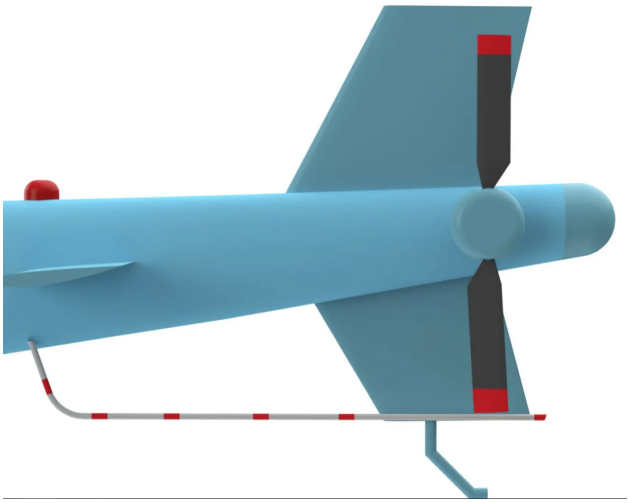

Figure 9.1: Vertical Stabilizer

Table 9.1: Vertical Stabilizer Design Specifications

Parameter	Value
Airfoil Cross-Section	NACA 4412
Angle of Incidence (°)	5
Surface Area [m^2 (ft^2)]	1.18 (12.7)
Upper Stabilizer Span [m (ft)]	0.96 (3.15)
Lower Stabilizer Span [m (ft)]	0.82 (2.69)
Root Chord [m (ft)]	0.82 (2.69)
Tip Chord [m (ft)]	0.50 (1.64)
Lever Arm from C.G. [m (ft)]	5.305 (17.405)
Spacing Ratio	0.45
Blockage Ratio	50%

specific geometry of the vertical fin with respect to the tail rotor disk area is illustrated below in Figure 9.1. In stable forward flight, the lever arm acting on the vertical fin is at 5.305 m (17.405 ft) from the center of gravity.

9.2 Horizontal Stabilizer Design

For the horizontal stabilizer, there were a few choices. *Draco* could use an asymmetrical inverted horizontal fin similar to a Robinson R22, "Case 1," or a horizontal fin forward of the tail rotor disk along the tail boom, "Case 2." Case 1 brings up some stability issues, primarily the tendency of the horizontal fin to induce rolling motion of the aircraft due to its asymmetry. In dire cases, such as low-G conditions, this could lead to instability issues, so Case 2 is the safer option for a passenger-carrying aircraft.

The downside of Case 2 is that the moment arm is reduced, requiring a larger surface area to provide the proper downward force to provide straight and level flight during the loiter phase. Taking the pitching moments and flight conditions of the loiter phase, we found the required amount of downward force with a moment arm of 4.24 m (13.9 ft) and a NACA4412 at 2° downward on the inverted airfoil would need a surface area of 0.217 m^2 (2.33 ft^2).

This design gives relief to the pilot by providing roll stability and straight, level flight during the loiter segment, and the symmetric horizontal fin configuration helps improve the dynamic stability during forward flight. The full empennage is shown in Figure 9.2.

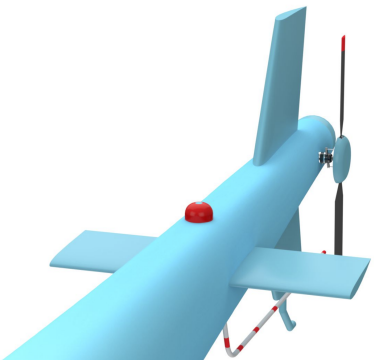

Figure 9.2: Empennage

10 Avionics and Controls

10.1 Mission Requirements

Draco is a Hydrogen-Electric VTOL aircraft that will pioneer the path forward in the field of sustainable flight. With this comes challenges to cockpit design that are not currently covered by the Code of Federal Regulations found in 14 CFR Part 27 [36], which would be the regulations for this type of rotorcraft due to Draco being under 7,000lbs and seating under nine passengers as per 14 CFR 27.1(a). So, while Draco is compliant with the Airworthiness Standards, the design team needed to create the needed standards for Hydrogen-Electric VTOL. The main objective of the mission is to extend the endurance of Draco's loitering time at the mission site. Most of all, decisions within the cockpit were seen through this mission lens while remaining CFR compliant.

10.2 Navigation

Draco utilizes all required navigation instruments listed in 14 CFR 27.1303 to include Vertical Speed Indicator, Airspeed Indicator, Altimeter, and Compass. These conditions are satisfied by the use of the Garmin GI 275 [37] in the "Attitude Indicator" configuration, displayed in Figure 10.1. This was selected based on the mission requirements, and having the absolute bare minimum in terms of instruments helps improve weight, thus increasing loiter time. *Draco* is certifiable for Visual Flight Rules (VFR) during day flight found in 14 CFR 91.205(b) [38]. But *Draco* is not certifiable for Instrument Flight Rules (IFR). These restrictions were made due to the mission requirements not needing night flight, nor stating IFR was required. These decisions helped reduce weight and power draw, such as positioning the lights, thus increasing the loiter endurance. For low-cost options, there is enough space for a standard set of steam gauges.

Figure 10.1: Navigation Panel, Garmin GI 275

10.3 Warning System

The future of Hydrogen-Electric VTOL is dependent on the premise that it is a safe alternative to conventional gas-powered VTOL. It will only take a few mishaps to drive away the public's perception of the technology, with a hydrogen tank rupture into an explosion being the most damaging to public opinion.

Draco is fitted with standard warning indicators listed in 14 CFR 27.1305 and 14 CFR 91.205(b). These are main/tail rotor high temperature, main/tail rotor metal contamination, main/tail gearbox oil pressure, low RPM, and starter on. There are some others that were taken from the same list but converted to meet Hydrogen-Electric VTOL requirements, low hydrogen to provide approximately 10 minutes of flight, and high hydrogen pressure.

These warning lights are labeled clearly along the top of the navigation panel, so they are within the core visual field of the pilot. The warnings are also audibly announced to the pilot in the form of a standard

alarm "beep" twice, followed up by a narrated voice stating the warning that was triggered, and this is then repeated until Silence is pressed. The warning light remains lit until it is no longer triggered. This method helps ensure pilot notification is confirmed and they are fully aware of the situation.

Figure 10.2: Warning Lights

10.4 Engine Monitoring

Below the navigation panel is where *Draco*'s engine panel is located, so it is still within the visual field of the pilot when their head is facing forward. The panel houses the Multi-Function Display (MFD) that displays the monitoring gauges for the engine, fuel tank, and fuel cells. The reason for the use of an MFD is due to the lack of aviation-rated gauges with proper calibration and labeling for hydrogen states. The MFD displays all the needed indicators required by 14 CFR 27.1305 and 14 CFR 91.205(b) that apply to *Draco*.

The indicators on the MFD are fuel cell current, hydrogen pressure, and quantity. As stated above, these hydrogen gauges are not present on the aviation market and thus will need to modify a standard Electric Flight Information System (EFIS) MFD to display our specific needs. The EDM-930 MFD was found to be programmable and able to display *Draco*'s hydrogen needs [39, 40]. This MFD also has less weight than a collection of the same instruments. The lighting switches, ignition, clutch switch, and master switch are also located on the engine panel. The dual tachometer is located on the navigation panel, though for a better visual of this indicator.

10.5 Communication

Draco's communication is handled by a Very High Frequency (VHF) radio system, GTR 225B [41], to satisfy 14 CFR 27.1457. This radio is placed in the avionics bay panel below the engine panel, along with the transponder GTX 325 [42] and the controller GMA350H [43]. The transponder is Mode C type but can be upgraded to include Mode A. The pilot can "mic-up" with a button on the cyclic handle. The antenna is placed on the bottom of the fuselage to provide an unobstructed beam path to the transmitting/receiving tower. The use of VHF and not including Ultra High Frequency (UHF) was decided it was not necessary to complete the mission and only added weight along with power needs.

10.6 Pilot's Visual Field

An important aspect of the cockpit is to ensure that the pilot is not unnecessarily looking around for information. To ensure this and reduce pilot fatigue, all important instruments and indicators are within the

Figure 10.3: Engine Panel: EDM-930 MFD

pilot's natural field of view when looking out into the horizon. By setting the rendering camera to that of a human eye, with a 20mm focal length, and positioning it where the pilot's eyes would be, we generated the pilot's perspective when looking directly ahead. In Figure 10.5, we see that the navigation and engine monitor are within the pilot's view. The communication is slightly out of view and requires the pilot to look down, but these instruments are less vital and do not need to be fully in view. Figure 10.4 also visualizes an external view of the cockpit, which has windows installed into the floor to allow for better observations of wildlife during the mission.

Figure 10.4: *Draco*'s Cockpit

Figure 10.5: Pilot's Cockpit View

10.7 Weight, Cost, and Power

Draco's avionics have a mass of only 6.6 kg (14.55 lb) and require a constant voltage supply of 14V, DC. The total cost of this system, including all aforementioned components, is $16,829. The compass does have a current draw, but the alternative of a liquid-filled magnetic compass has problems of leaking and thus was excluded.

10.8 Heating and Cooling

Draco's heating for the pilot is supplied by siphoning off heat produced by the chemical reaction of the fuel cells through a small heating exchanger to heat cabin air. This gives comfort to the pilot and reduces pilot fatigue. The cooling is handled with a small air vent in the nose and small hatch windows on the doors that can be opened to allow fresh air to cycle through the cockpit. These air conditioning features follow the 14 CFR 27.859 standard.

11 Weight and Balance

11.1 Weight Breakdown

Draco's gross takeoff weight is 1417 kg (3124 lb). Subtracting the 14.8 kg (31.3 lb) of hydrogen, 24.1 kg (53.13 lb) of coolant, and 185 kg (407.86 lb) payload, the empty weight is 1193.1 kg. A detailed breakdown of system weights is shown in Table 11.1.

11.2 Center of Gravity Analysis

Every component is placed to keep the center of gravity in line with the main rotor shaft at takeoff. The vertical position of the center of gravity is 0.4985 m (1.635 ft) above the bottom of the landing gear, and the lateral and longitudinal center of gravity are exactly in line with the main rotor shaft. During the mission, only the fuel weight depletes. The hydrogen tanks are centered about the vehicle's C.G. to ensure that the longitudinal C.G. minimally changes throughout the mission. This symmetry allows for zero change in lateral

Table 11.1: Vehicle Weight Breakdown

System Component	Weight [kg (lb)]	System Component	Weight [kg (lb)]
PEMFC Stack	**100.8 (222.23)**	**Power and Transmission**	**152.3 (335.8)**
Air System	**22.62 (49.87)**	Tail Drive Shaft	6.13 (13.51)
Humidifier	7.05 (15.54)	Main Drive Shaft	13.9 (30.64)
Mass Flow Meter	9.5 (20.94)	Gearbox Housing	26.47 (58.4)
Blower	4.97 (10.96)	Main Gears and Pinions	17.98 (39.64)
Deionizer	1.1 (2.43)	Electric Motors	87.8 (193.6)
High-Temperature Cooling System	**41.84 (92.24)**	**Main Rotor**	**175.2 (386.3)**
Radiator	5.93 (13.07)	Articulated Hub	95.3 (210.0)
Coolant	24.1 (53.13)	Main Rotor Blades	57.1 (125.8)
Fan	2.5 (5.51)	Hub cap	22.82 (50.30)
Tank	5.33 (9.55)		
Pump	2.76 (6.08)	**Tail Rotor**	**21.28 (46.91)**
Filter	0.41 (0.90)	Tail Rotor Hub and Cap	10.88 (23.99)
Regulator	0.41 (0.90)	Tail Rotor Blades	10.4 (22.93)
Power	0.41 (0.90)	**Structures**	**446.4 (984.1)**
Electrical	**66.72 (147.09)**	Fuselage Structure	178.7 (394.0)
Controller	6.72 (14.82)	Wings	60.4 (133.2)
Battery (with casing)	30 (66.14)	Empennage	45.47 (100.2)
DC/DC Converter	30 (66.14)	Windshield	23 (50.7)
Hydrogen Supply System	183.4 (404.33)	Landing Gear	34.83 (76.79)
Tanks	175 (385.8)	Skin	70.91 (156.3)
Pressure regulators	3.6 (7.94)	Seats	33.1 (73.1)
Pressure relief valves	2.4 (5.3)	**Avionics**	**6.6 (14.55)**
Fuel	**14.8 (31.3)**	**Payload**	**185 (407.9)**
PEMFC System Total	**430.18 (948.4)**	**GTOW**	**1417 (3124)**

C.G. throughout the mission. The longitudinal and vertical C.G. travel a total of 0.115 mm (0.004 in) aft and 2.7 mm (0.11 in) up, respectively, throughout the mission. These changes have a negligible impact on the performance and structural stability. The shift in C.G. per mission segment is directly proportional to the percentage of hydrogen consumed. Both the weight and center of gravity evolution throughout the mission are visualized in Figure 11.1.

12 Vehicle Performance

Draco was designed for maximized time in loiter during its mission. The exceptional lift-to-drag ratio in this phase of flight can be attributed to the optimized aerodynamic design of each individual component of the vehicle.

12.1 Component-Wise Drag Estimation

A significant source of power consumed during forward flight can be classified as parasitic power, which is directly correlated to the vehicle drag. The drag coefficient of each individual component was estimated using Prouty's published method for classical helicopter drag estimations [44]. The wetted area for each component was directly taken from its corresponding CAD model. Dimensional component drag was directly calculated from these values and is shown in Table 12.1. A 10% increment due to component interference, along with a 5% increment due to miscellaneous parts such as pitot tubes and antennas, was added to the overall drag estimations, as recommended by Prouty. The estimated flat plate area for *Draco* then becomes 0.422 m^2 (4.542 ft^2).

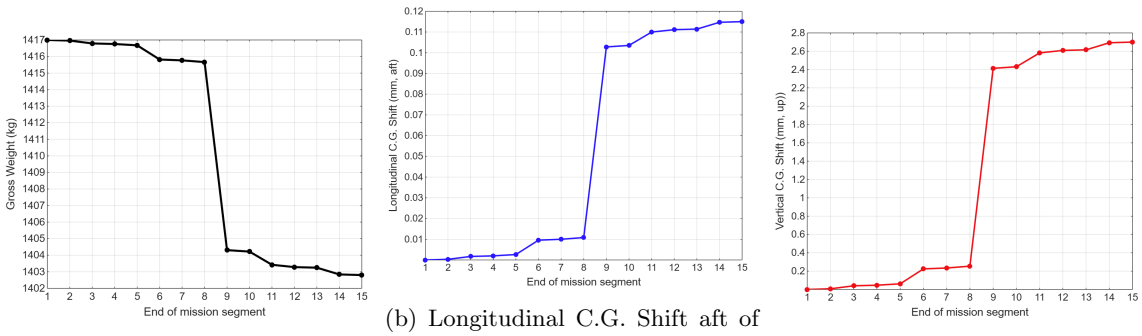

(a) Weight Evolution

(b) Longitudinal C.G. Shift aft of Main Rotor Shaft

(c) Vertical C.G. Shift

Figure 11.1: Weight Center of Gravity Evolution Throughout Sizing Mission

Table 12.1: Component-Wise Drag and Flat Plate Area

Component	**Drag Coefficient**	**Flat Plate Area**	
		m^2	**ft^2**
Fuselage	0.044	0.093	1.001
Wing	0.008	0.017	0.183
Main Rotor Hub	0.801	0.121	1.302
Tail Rotor Hub	0.199	0.024	0.258
Landing Gear	0.403	0.081	0.872
Horizontal Stabilizer	0.019	0.005	0.054
Vertical Stabilizer	0.019	0.005	0.054
Interference (10%)	0.149	0.051	0.549
Miscellaneous (5%)	0.075	0.025	0.269
Total	**1.717**	**0.422**	**4.542**

12.2 Hover Download

Rotor wash is a common phenomenon that has a significant impact on lift-compound aircraft designs. During hover, the rotor must generate enough thrust not only to support the gross takeoff weight but also to counteract the additional downforce caused by rotor wake impinging on the fuselage and wings. These download effects were estimated by integrating the local drag coefficient with the sectional width of the affected surfaces. For this design, the rotor-induced download was estimated to be approximately 12% of the total lift requirement.

12.3 Hover Performance

Draco is optimized for maximum efficiency during cruise flight, but hover performance remains a critical consideration for any vertical lift aircraft. Hovering demands some of the highest power levels within *Draco*'s operational envelope. Because key components of *Draco*'s powerplant are sized based on peak power requirements, reducing this maximum demand is essential to lowering the vehicle's empty weight fraction and improving overall performance.

Draco demonstrates strong hover performance, as illustrated in Figure 12.1, exceeding the RFP requirement of maintaining hover up to 60 meters. This capability enables *Draco* to perform missions beyond the original scope, including operations with heavier payloads and in higher temperature environments. Notably, *Draco*'s hover ceiling is constrained by the power available in the onboard energy system rather than by aerodynamic limitations such as blade stall or mechanical constraints like transmission limits.

12.4 Airframe Aerodynamic Metrics

As specified in the RFP, the aerodynamic properties of the airframe, which excludes the wings, blades, and empennage, are summarized below in Table 12.2. For the airframe pitching moment volume, we found

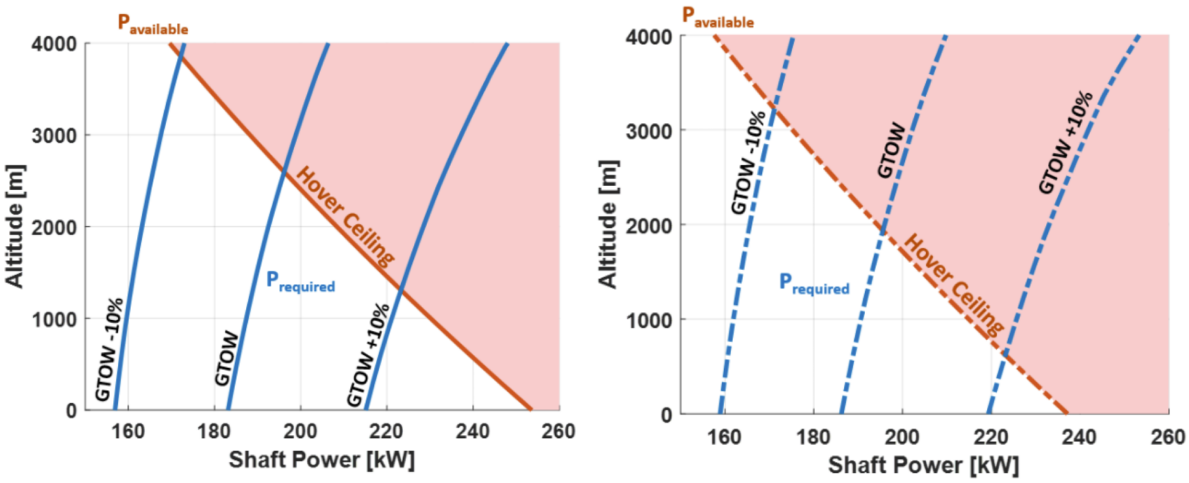

(a) ISA (b) ISA +20°C

Figure 12.1: Hover Altitude vs. Required and Available Shaft Power for Range of Gross Weights

modeled our fuselage geometry as a high-thickness, low camber airfoil. At 0° pitch and yaw angle, *Draco*'s airframe shape is similar to the NACA 2415 at a -3° angle of attack, which gives a pitching moment coefficient of about -0.14 [45]. The pitching moment volume M/q can be calculated as $M/q = C_m Sc$. Based on the top-view area projection of the fuselage and the end-to-end distance between the nose and tail boom, we estimate that $S = 6.62m^2 = 71.26ft^2$, and $c = 9.17m = 30.09ft^2$. When applied to drag area calculations, we calculated a drag area (D/q) of 0.166 m^2 (1.78 ft^2), which is significantly less than the flat plate area. For safety, we assume the more conservative estimate of drag area calculated with Prouty's method.

Table 12.2: Airframe Aerodynamic Metrics

Metric	Value
Drag Area (D/q) [m^2 (ft^2)]	0.422 (4.542)
Pitching Moment Volume (M/q) [m^3 (ft^3)]	-3.521 (-124.3)

12.5 Forward Flight Performance

The RFP asks us to optimize our vehicle for maximum time in loitering flight. *Draco* was designed with this in mind, keeping each component's drag to a minimum for superior cruise performance.

Draco's forward flight performance was evaluated at its design gross takeoff weight (GTOW) of 1413 kg (3076 lbs). Figure 12.2 illustrates how power required varies with forward speed at a loiter altitude of 60 meters (197 feet). To highlight the effects of configuration changes, both a modified single-main-rotor (SMR) *Draco* and the final lift-compound design are modeled. The addition of wings and a reduction in rotor tip speed distinguish *Draco*'s final configuration from the original SMR setup. While the lower tip speed increases the advance ratio, raising the main rotor's profile power requirement, the wings offload the rotor in forward flight, significantly reducing induced power. This comes at the cost of increased parasitic power due to additional drag. To optimize mission efficiency, *Draco* is designed to operate at the velocity for best endurance (V_{BE}) during loiter and at the velocity for best range (V_{BR}) during cruise, which are labeled in Figure 12.3.

The lift-to-drag ratio (L/D) serves as a valuable metric for assessing Draco's aerodynamic efficiency relative to alternative configurations. Figure 12.4 presents the L/D performance across a range of airspeeds at a 60-meter loiter altitude for both the final Draco lift-compound design and the modified single-main-rotor (SMR) variant. At higher speeds, Draco's forward tilt increases wing lift but also raises fuselage drag, reducing L/D. While the SMR design is more efficient at high speeds, making it better suited for cruise-dominated missions, the lift-compound Draco shows superior L/D in low-speed flight. This makes it more effective for hover-adjacent operations such as loitering, where aerodynamic efficiency at low airspeeds is critical.

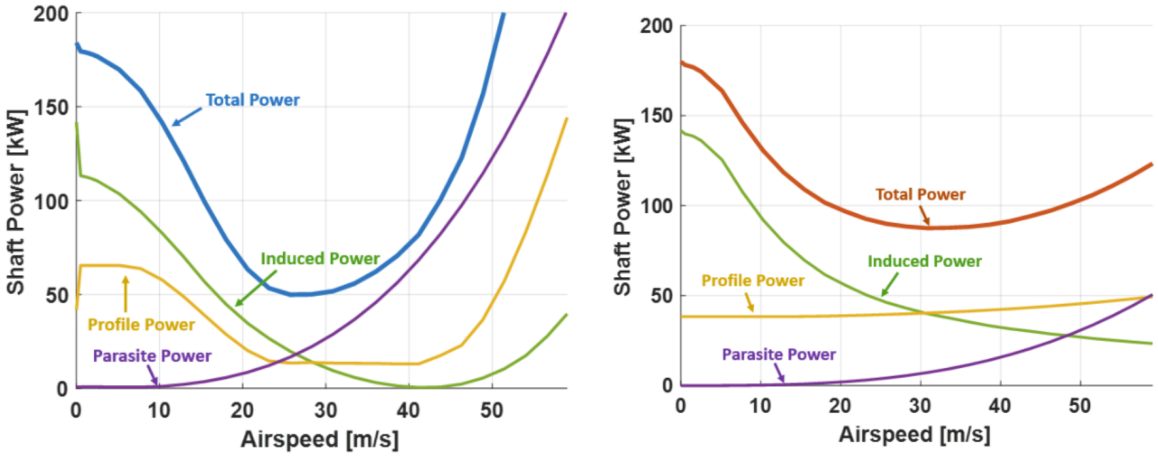

(a) *Draco* (b) SMR Counterpart

Figure 12.2: Required Shaft Power vs. Airspeed at GTOW

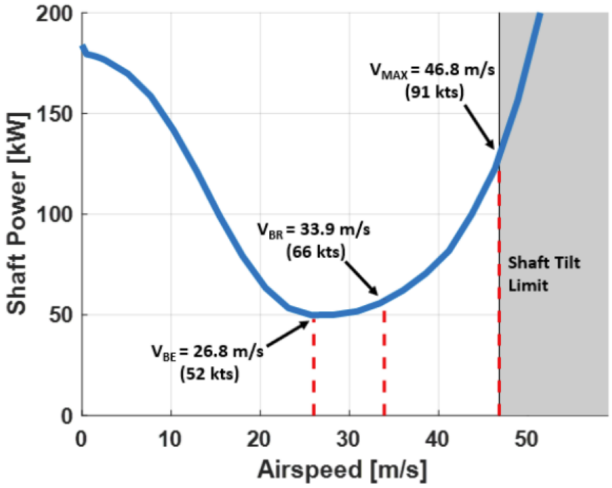

Figure 12.3: *Draco* Power vs. Airspeed from HOGE to Maximum Level Flight Speed

12.6 Mission-Specific Performance

Draco is sized specially for the mission outlined by the RFP, and every system is designed to optimize its performance and maximize its loiter time during the mission. The performance analysis revealed significant improvements in the sizing of mission power requirements, particularly during the cruise and loiter segments. This reduction of power and hydrogen flow rate allows for longer loiter endurance for the same hydrogen storage.

For safety, we avoid underestimating the most extreme power requirements. We maintained a more conservative power estimate in hover and vertical climb from our sizing methodology.

Also, because our initial sizing did not account for the available hydrogen supply, it underestimated our hydrogen storage capacity. As stated in Section 5: PEMFC System Design, *Draco* can store up to 14.8 kg (32.62 lb) of hydrogen, but about 95%, or 14.2 kg (31.3 lb), is usable. By designing for 14.2 kg (31.3 lb) of global hydrogen consumption throughout the mission, we extended our loiter time further.

After implementing these changes, *Draco*'s full potential is unlocked. *Draco*'s official loiter endurance is **190 minutes and 18 seconds**. Alternatively, this loiter time may be reduced to allow for fuel reserves, depending on the pilot's preference. Without including the fuel reserves, *Draco*'s full mission-specific performance is outlined in Table 12.3.

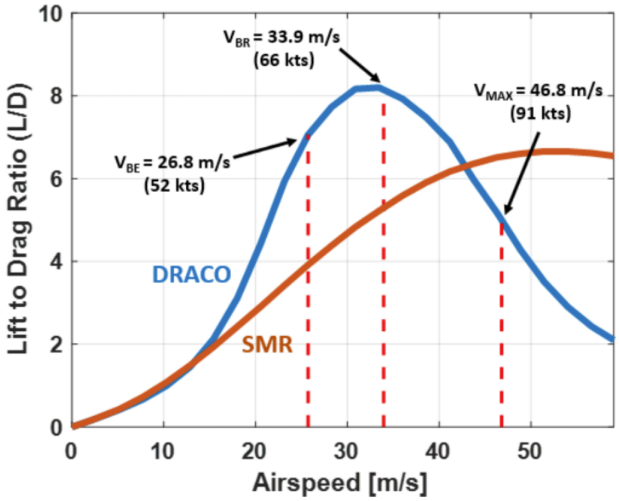

Figure 12.4: L/D vs. Airspeed for *Draco* and SMR Counterpart

As requested by the RFP, we calculated the horizontal speed during steady climbs, steady or steep descents, and forward flight. This data is provided for segments 5, 6, 7, 8, 9, 10, and 12.

Segment 1, the vertical takeoff, is omitted from this analysis because the duration and power draw depend on the pilot's preference. As for Segment 16, the duration of the landing depends on the pilot's preference, so this can be adjusted.

The data in Table 12.3 confirms that *Draco* consumes 14.2 kg (31.3 lb) throughout the mission and requires an installed power of 254.4 kW (341.1 hp).

13 Safety

We designed *Draco* according to U.S. federal regulations (14 CFR 27) and EU certification requirements for small rotorcraft (CS-27) [36, 46]. Considering the new form of propulsion we are using, we had to translate these requirements into ways that pertain to hydrogen propulsion. In particular, 14 CFR 27 has rules for conventional engine rotorcraft fuel storage that are applicable to hydrogen, including impact resistance and hot weather operations. Because our fuel is a high-pressure gas, we emphasized tank safety in our design by using reliable and market-ready type 4 cylinders that are rated to reach the maximum allowed pressure by the RFP.

We also designed our avionics system with 14 CFR 27 in mind, but we needed to add considerations that are specific to our propulsion system. We added warning lights and indicators for stack pressure, humidity, temperature, and power output.

Aside from our propulsion system, we designed the rest of the vehicle with 14 CFR 27 and CS-27 in mind. All warning systems, engine monitoring, navigation systems, and structures were designed to meet the specified requirements set by these regulations and the RFP. CS-27 also requires that we provide hover and forward flight performance, which we include in section 12.

While the RFP allows us to assume favorable conditions of ISA with no wind speed, CS-27 requires that takeoff may not require exceptional piloting skill or exceptionally favorable conditions [46]. Further testing should be conducted on *Draco* in real-life conditions to ensure it meets certification requirements.

14 Cost Breakdown

We implemented the Harris-Scully model for *Draco*'s life cycle cost analysis, which is based on real-life helicopter data, analyzed in the NDARC report [3]. These models use data from 1994, so we implemented

Table 12.3: Mission-Specific Performance Data

Mission segment	Duration [min]	Horizontal Speed [m/s (ft/s)]	Aerodynamic Power [kW(hp)]	Total Power [kW(hp)]	Transmission Efficiency
2	0.25	0	142.6 (191.2)	146.9 (197.0)	96%
3	1.21	0	246.9 (331.0)	254.4 (341.1)	96%
4	0.17	0	237.8 (319.0)	245.1 (328.7)	96%
5	0.91	V_{climb}, 27.88 (91.47)	79.40 (106.5)	81.81 (109.7)	96%
6	13.07	V_{br}, 33.90 (111.22)	55.21 (74.04)	56.89 (76.29)	96%
7	0.59	V_{climb}, 27.88 (91.47)	78.88 (105.8)	81.28 (109.0)	96%
8	0.50	0	237.4 (318.4)	244.7 (328.1)	96%
9	**190.30**	V_{be}, 26.80 (87.93)	48.40 (64.90)	49.87 (66.88)	96%
10	1.01	V_{climb}, 28.02 (91.93)	79.02 (106.0)	81.42 (109.2)	96%
11	12.13	V_{br}, 33.90 (111.22)	55.21 (74.04)	56.89 (76.29)	96%
12	1.62	$V_{descent}$, 28.22 (92.59)	79.26 (106.3)	81.67 (109.5)	96%
13	0.17	0	235.3 (315.5)	242.4 (325.1)	96%
14	1.84	0	243.7 (326.9)	251.2 (336.8)	96%
15	0.25	0	140.9 (189.0)	145.2 (194.7)	96%
16	N/A	0	60.60 (81.26)	62.44 (83.73)	96%

Mission segment	Electric Motor RPM	Electric Motor Torque [N*m(lb*ft)]	PEMFC Efficiency	Hydrogen Flow Rate [kg/min (lb/min)]	Hydrogen Consumption [kg (lb)]
2	2500	544.6 (401.6)	36.49%	0.154 (0.340)	0.039 (0.085)
3	2500	942.9 (695.5)	32.19%	0.141 (0.311)	0.170 (0.375)
4	2500	908.5 (670.1)	34.29%	0.209 (0.461)	0.035 (0.077)
5	1650	459.5 (338.9)	35.77%	0.088 (0.193)	0.079 (0.175)
6	1650	319.5 (235.7)	33.23%	0.066 (0.145)	0.857 (1.890)
7	2500	301.3 (222.2)	35.73%	0.087 (0.192)	0.052 (0.114)
8	2500	907.0 (668.9)	34.34%	0.208 (0.459)	0.104 (0.229)
9	1650	280.1 (206.6)	32.02%	0.060 (0.132)	11.357 (25.038)
10	1650	457.3 (337.3)	35.74%	0.087 (0.192)	0.089 (0.195)
11	1650	319.5 (235.7)	33.23%	0.066 (0.145)	0.796 (1.755)
12	1650	458.7 (337.3)	35.76%	0.088 (0.193)	0.142 (0.313)
13	2500	898.8 (662.9)	34.56%	0.205 (0.451)	0.034 (0.075)
14	2500	931.0 (686.7)	33.40%	0.222 (0.489)	0.407 (0.898)
15	2500	538.3 (397.1)	36.53%	0.152 (0.336)	0.038 (0.085)
16	1650	350.7 (258.7)	34.00%	0.070 (0.155)	N/A

a scaling factor of 2.16 to account for inflation of U.S. Dollars (USD) between 1994 and 2025. All costs provided are in terms of 2025 U.S. dollars.

14.1 Base Price

Using the NDARC model, we can rewrite its cost prediction equations in terms of empty weight, useful load (gross weight minus empty weight), disk loading, hover figure of merit, installed power, number of blades, and air density. From *Draco*'s specifications and the NDARC model, we predict a base price of $1,380,961 in 2025 USD.

14.2 Other Costs

Like any other helicopter, operating *Draco* comes with additional maintenance costs, direct, and indirect operating costs. NDARC theory allows us to predict the maintenance costs based on empty weight and installed power. From this, plus the scaling factors for inflation and PEMFC, we predict a maintenance cost of $584.91 per flight hour.

Lastly, we used the same methods to predict a total operating cost of $306,137 per year of operation, assuming one flight per day. Direct operating costs of refueling amount to about $86,432 per year, assuming one flight per day, based on 2024 hydrogen prices [47]. Indirect operating costs, including pilot salary, management personnel, buildings, insurance, and depreciation over time, amount to about $219,705, 71.8% of the operating costs.

15 Summary

The University of Maryland Undergraduate Team is proud to present *Draco* as our response to the RFP of the 42nd Annual VFS Student Design Competition. With excellent aerodynamic performance and installed power capabilities of the novel PEMFC system, *Draco* achieves a loiter endurance of 190 minutes and 18 seconds, ensuring a safe, enjoyable experience for both pilot and passenger. Every system is fully integrated and designed to address all challenges associated with this new technology.

- *Draco* is designed with proven, safe, and mechanically simple technology, minimizing technological risk while implementing the novel PEMFC system.
- Compounded wings provide additional lift during loiter to offload the main rotor during loiter. This reduces power requirements by 49.4% during loiter and 58.6% during cruise, which are the majority of mission time. This significantly extends *Draco*'s loiter endurance.
- The PEMFC, transmission, avionics, and structures are designed for the pilot's and passenger's safety as a central priority, with special attention given to flight-critical failure modes.
- The fully-articulated rotor hub with elastomeric bearings allows for easy control of flight and hover, and transition between mission segments.
- Aerodynamically designed landing gear, rotor hubs, and airframe minimize drag and reduce power requirements further.
- The two redundant motors supply the needed torque and power for all mission segments, and one motor provides enough power for a steady descent in case of one engine inoperative.
- The added buffer battery supplies the power needed for high-intensity, short-duration hover and vertical climb mission segments, to save on power demands and weight of the PEMFC system. It recharges during low-intensity mission segments in preparation for the next segments.

Figure 15.1: *Draco*

References

[1] Aurora Flight Sciences: A Boeing Company. *SKIRON-XLE Completes 7-Hour Endurance Flight*. URL: https://www.aurora.aero/2024/08/27/skiron-xle-completes-7-hour-endurance-flight/. (accessed: 01.29.2025).

[2] *Robinson R44 Maintenance Manual*. 2006.

[3] Wayne Johnson. "NDARC: NASA Design and Analysis of Rotorcraft". In: *NASA-TP 20220000355* (2023).

[4] Rolls Royce. *RR300 — Rolls Royce*. URL: https://www.rolls-royce.com/products-and-services/civil-aerospace/helicopters/rr300.aspx#/. (accessed: 12.04.2024).

[5] Fuel Cells Works. *Horizon Automotive PEM Fuel Cells to Set 300kW Benchmark*. URL: https://fuelcellsworks.com/news/horizon-automotive-pem-fuel-cells-to-set-300kw-benchmark. (accessed: 10.26.2024).

[6] About Energy. *The Tesla 4680: Does Size Matter?* URL: https://www.aboutenergy.io/post/the-tesla-4680-does-size-matter. (accessed: 04.09.2025).

[7] Hyeonsoo Yeo and Wayne Johnson. "Prediction of Maximum Lift Capability of Helicopter Rotors". In: *Journal of Aircraft* 52.1-9 (2015). DOI: https://doi.org/10.2514/1.C032693.

[8] Anubhav Datta. *PEM Fuel Cell Model for Conceptual Design of Hydrogen eVTOL Aircraft*. Tech. rep. NASA, 2021.

[9] C. Balaji, Balaji Srinivasan, and Sateesh Gedupudi. "Heat Transfer Engineering: Fundamentals and Techniques". In: *Academic Press* 199-231 (2021). DOI: https://doi.org/10.1016/B978-0-12-818503-2.00007-1.

[10] Raghu Krishna Moorthy and Soumitra Biswas. "Compact Heat Exchangers – Technology Design Analysis". In: *The Scitech Journal* 3 (2016).

[11] Mohamed El-sayed Gomaa. "Experimental And Numerical Investigations On The Automotive Radiator Performance Using Louvered-Fin Heat Exchanger". In: *Journal of Engineering Studies* 37.345-362 (2009).

[12] Boyd Welding LLC. *5 Gallon 12x8x12 Aluminum Tank — Boyd Welding LLC*. URL: https://fueltankparts.com/products/5-gallon-universal-12-x-8-x-12. (accessed: 3.27.2025).

[13] SPAL Automotive. *Axial Fans with Brushless Motor 12V/24V DC-SPAL*. URL: https://www.spalautomotive.com/en/brushless-axial-fans?productcode=VA113-BBL504P/N-94A&articleid=71106. (accessed: 4.01.2025).

[14] SPAL Automotive. *12V-24V Coolant Pumps — SPAL*. URL: https://www.spalautomotive.com/en/coolant-pumps. (accessed: 3.27.2025).

[15] Rotron / Airscrew. *Rotron AXIMAX 1 Small Vaneaxial Fans*. URL: https://www.rotron.com/-/media/ametekrotron/products/digital-library/table-of-contents/centraxial-blowers/11-06_centrimil.pdf?dmc=1&la=en&hash=9DD084A2A61B90656611A9A75A5090C8. (accessed: 4.12.2025).

[16] Fumatech. *Humidifier Modules Ecomate: Fumatech*. URL: https://www.fumatech.com/en/products/humidifier-modules-ecomate/. (accessed: 5.01.2025).

[17] Hyfindr. *Ion Exchange Filter IonFree (High Capacity) — Hyfindr*. URL: https://hyfindr.com/en/shop/products/ion-exchange-filter-ionfree-high-capacity. (accessed: 05.19.2025).

[18] Bronkhorst. *IN-FLOW Series: Rugged Industrial Flow Meters*. URL: https://www.bronkhorst.com/products/gas-flow/in-flow/?model=F-106DI. (accessed: 05.17.2025).

[19] Hyfindr. *ILJIN Hysolus on B2B Marketplace for Hydrogen Economy — Hyfindr*. URL: https://hyfindr.com/en/store/ILJIN-Hysolus. (accessed: 11.05.2024).

[20] EMERSON. *TESCOM Series HV-7000 Onboard Regulator PDF*. URL: https://www.emerson.com/documents/automation/flyer-hv-7000-series-hydrogen-onboard-regulator-tescom-en-10191298.pdf. (accessed: 05.05.2025).

[21] Pressure Tech Ltd. *LW351 Datasheet PDF*. URL: https://www.pressure-tech.com/files/124/LW351%20Datasheet.pdf. (accessed: 04.19.2025).

[22] Hyfindr. *Hydrogen Pressure Relief Valve - Series 492 — Hyfindr*. URL: https://hyfindr.com/en/shop/products/hydrogen-pressure-relief-valve-series-492. (accessed: 05.17.2025).

[23] Hyfindr. *Safety Relief Valves - Series 946 — Hyfindr*. URL: https://hyfindr.com/en/shop/products/enclosed-discharge-safety-relief-valves-type-946-threaded. (accessed: 05.17.2025).
[24] Aradex. *DC/DC Converter VP5000 - ARADEX AG*. URL: https://www.aradex.de/en/vectopower/dc-dc-converter-vp5000/. (accessed: 4.05.2025).
[25] Bosch. *Fuel cell control unit*. URL: https://www.bosch-mobility.com/en/solutions/powertrain/fuel-cell-electric/fuel-cell-control-unit/. (accessed: 05.19.2025).
[26] Emrax: Innovative E-Drives. *EMRAX 348 (400 kW — 1000Nm)*. URL: https://emrax.com/e-motors/emrax-348/. (accessed: 03.19.2025).
[27] Evolito Ltd. *Axial Flux Motors - Electric Motors For Aerospace*. URL: https://evolito.aero/axial-flux-motors/. (accessed: 03.19.2025).
[28] Timothy J. Lisle et al. "Bending fatigue strength of aerospace quality gear steels at ambient and elevated temperatures". In: *International Journal of Fatigue* 164.1 (2022). DOI: https://doi.org/10.1016/j.ijfatigue.2022.107125.
[29] Darle W. Dudley and Stephen P. Radzevich. *Dudley's Handbook of Practical Gear Design and Manufacture, Second Edition*. CRC Press, 2012.
[30] Robert C. Juvinall. *Engineering Considerations of Stress, Strain, and Strength, First Edition*. McGraw-Hill, Inc., 1967.
[31] KHK Stock Gears. *Calculation of Gear Dimensions*. URL: https://khkgears.net/new/gear_knowledge/gear_technical_reference/calculation_gear_dimensions.html. (accessed: 03.19.2025).
[32] Dr. Tomasz Krysinski. "Drive Shafts". Presented to UMD Students on 02.19.2025.
[33] Dr. Tomasz Krysinski. "Dynamic Optimization of Shaft Lines". Presented to UMD Students on 02.12.2025.
[34] Michael Ashby. *Materials Selection in Mechanical Design*. Fifth Edition. Butterworth-Heinemann, 2018.
[35] James E. Young. "Helicopter Vertical Stabilizer Design Considerations". MA thesis. Naval Postgraduate School, 1983.
[36] 14 C.F.R. Part 27.
[37] Garmin. *GI 275: Attitude Indicator*. URL: https://www.garmin.com/en-US/p/719027/. (accessed: 2.01.2025).
[38] 14 C.F.R. Part 91.
[39] Sarasota Avionics. *JP Instruments EDM-930 Primary*. URL: https://sarasotaavionics.com/avionics/edm930-certified?srsltid=AfmBOoqS8hDLmgetePBi0JtxlzDDhCj6kf4JBPB95zo1VbTtCCUPnIkF. (accessed: 11.05.2024).
[40] Aircraft Spruce & Specialty Co. *JPI EDM-930 Primary Certified Engine Monitor*. URL: https://www.aircraftspruce.com/catalog/inpages/jpi930.php. (accessed: 11.05.2024).
[41] Sea Aerospace. *GI 225B: VHF Comm*. URL: https://www.seaerospace.com/sales/product/Garmin/GTR-225B?srsltid=AfmBOorrogpWa37xydmXA7NuiT3IeHu8bfpt2r7l9DSLphHs_Ped30tw. (accessed: 11.05.2024).
[42] Garmin. *GI 325: Mode C Transponder*. URL: https://www.garmin.com/en-US/p/117100/. (accessed: 11.05.2024).
[43] Garmin. *GMA 350H: Comm Controller*. URL: https://www.garmin.com/en-US/p/71339/pn/010-00871-31/. (accessed: 11.05.2024).
[44] Ray W. Prouty. *Helicopter Performance, Stability, and Control: 1st Edition*. Krieger Publishing Company Inc., 1986.
[45] James F. Marchman III. *Aerodynamics and Aircraft Performance, 3rd edition*. Independently Published in association with the Open Education Initiative of University Libraries at Virginia Tech, 2022.
[46] European Union Aviation Safety Agency. "Certification Specifications for Small Rotorcraft (CS-27)". In: *EASA* (2023).
[47] Ted McKlveen and Bav Roy. *The hidden 85%: How to make hydrogen cost-effective*. URL: https://www.weforum.org/stories/2024/05/hydrogen-hidden-costs-energy-transition/. (accessed: 05.25.2025).
[48] Rui Yin, Jing Huang, and Zhi-Yuan He. "Lift and Drag Coefficient Map of NACA4415 Airfoil". In: *Journal of Physics: Conference Series* (2021). DOI: https://doi.org/10.1088/1742-6596/2076/1/012066.

[49] Solvay. *Torlon PAI Design Guide: Specialty Polymers*. URL: https://drakeplastics.com/wp-content/uploads/2020/01/Torlon-PAI-Design-Guide_EN-227547.pdf. (accessed: 03.19.2025).
[50] Dr. Tomasz Krysinski. "Short Course of Transmission Design". Presented to UMD Students on 03.19.2025.
[51] Wanyi Ng, Mrinalgouda Patil, and Anubhav Datta. "Hydrogen Fuel Cell and Battery Hybrid Architecture for Range Extension of Electric VTOL (eVTOL) Aircraft". In: *Journal of the American Helicopter Society* 66 (2021).
[52] Wanyi Ng and Anubhav Datta. "Hydrogen Fuel Cells and Batteries for Electric-Vertical Takeoff and Landing Aircraft". In: *Journal of Aircraft* 56.5 (2019). DOI: https://doi.org/10.2514/1.C035218.
[53] Wanyi Ng. "An Experimental and Analytical Investigation of Hydrogen Fuel Cells for Electric Vertical Take-Off and Landing (eVTOL) Aircraft". MA thesis. University of Maryland, 2019.
[54] Vishwas V. Wadekar. "Heat Exchangers in Process Industry and Mini- and Microscale Heat Transfer". In: *Enhanced, Compact, and Ultra-Compact Heat Exchangers*. 2005.
[55] Dr. Tomasz Krysinski. "Engines: Electric Engines vs. Thermal Engines". Presented to UMD Students on 03.27.2025.